Iron and silicon isotope fractionation in silicate melts using first-principles molecular dynamics.

S. RABIN[1,2], M. BLANCHARD[1], C. PINILLA[3], F. POITRASSON[1], M. GREGOIRE[1]

[1]Géosciences Environnement Toulouse, Université de Toulouse, CNRS, IRD, UPS, CNES, 14-16, av. E. Belin, 31400 Toulouse, France

[2] Vrije Universiteit Brussel, Analytical, Environmental, and Geo-Chemistry, Pleinlaan 2, 1050 Brussels, Belgium (segolene.rabin@vub.be)

[3] Departamento de Fisica y Geociencias, Universidad del Norte, Barranquilla, Colombia

ABSTRACT

The direct determination of silicate melts iron and silicon isotopes signature remains a major challenge of high-temperature isotope geochemistry. For this reason, melts are often approximated by silicate glasses. Calculation of precise equilibrium Si and Fe isotopes fractionation factors between minerals and melt would indeed allow us to distinguish equilibrium fractionation from diffusion-driven kinetic fractionation involved in the iron and silicon isotopes signatures of Earth and other planets. In this study, we use for the first time, first-principles molecular dynamics based on density functional theory to determine iron and silicon isotope compositions of different silicate melts, namely: iron-rich basalt, iron-depleted basalt, basanite, trachyte and phonolite. The $^{57}Fe/^{54}Fe$ reduced partition function ratios (β-factors) of the different melts span over a 1.1 ‰ range at 1000 Kelvin (K) while $^{30}Si/^{28}Si$ β-factors are much less influenced by the melt composition with a 0.5 ‰ fractionation range at the same temperature. The main parameter controlling iron isotope fractionation in silicate melts having similar iron oxidation state is, after temperature, the average Fe-O bond length. The chemical environment around iron (e.g. Fe-Fe distances) is suggested to contribute to Fe isotope fractionation as well. Silicon isotopes fractionation seems also affected, but to a lesser extent, by its local chemical composition with decreasing Si-Fe distances leading to slightly higher Si β-factor in the melt. From these melts Fe and Si β-factors, a new set of equilibrium fractionation factors between a variety of minerals and melts has been calculated. These new $\Delta^{57}Fe_{min\text{-}melt}$ and $\Delta^{30}Si_{min\text{-}melt}$ sets allow us to discuss whether processes such as fractional crystallization, partial melting and diffusion could be responsible for the documented Fe and Si isotopes variations in igneous rocks. Our results suggest that: 1) fractional crystallization may explain at least part of the Fe and Si isotopic evolution during magmatic differentiation, for values up to $\delta^{57}Fe$ = 0.65 ‰ and $\delta^{30}Si$ = -0.1 ‰, respectively, 2) partial melting of the upper mantle can produce the Mid-Ocean Ridge Basalts (MORB) iron isotopes signature. Finally, we calculated that olivine at equilibrium with a basaltic melt could display an iron isotope composition down to -0.1 ‰ for $\delta^{57}Fe$. Hence, the lower isotopic compositions ($\delta^{57}Fe$ < -0.1 ‰) observed in natural olivines are most likely due to diffusion-driven kinetic fractionation.

Keywords: Density Functional Theory (DFT); Silicate melts; Isotope fractionation; Magmatic differentiation

1- INTRODUCTION

Understanding the detailed structural properties of iron-bearing silicate melts as well as the behavior of the constituting cations remains one of the great challenges in geosciences and in the glass-making industry. Many experimental and theoretical studies on melts from simple composition to natural-like melts have been carried out showing that cations could be either network former or network modifier depending on the nature of the cations and their coordination number (CN) that are dependent also of pressure, temperature and redox state of the melt (McMillan, 1984; Oestrike et al., 1987; Stein and Spera, 1996; Gerlach et al., 1998; Rossano et al., 2000; Jackson et al., 2005; Guillot and Sator, 2007b; Guillot and Sator, 2007a; Karki, 2010; Angeli et al., 2011; Bauchy and Micoulaut, 2011; Le Losq et al., 2014; Bajgain et al., 2015; Karki, 2015; Kim et al., 2016; Ghosh and Karki, 2018; Caracas et al., 2019; Solomatova and Caracas, 2019; Ghosh and Karki, 2020; Solomatova and Caracas, 2021). Silicon in melt is mostly four-fold coordinated and acts as the main network former of the melt structure. Despite the fact that silicon could be found as Si^0 in metallic inclusions of meteorites and planetary cores (Poitrasson, 2017), silicon is considered as only tetravalent in the upper mantle and crust of the Earth. Hence, silicon is not redox sensitive in terrestrial melts whereas iron is. Iron in melts has been assessed to behave differently in the melt depending on its redox state (Fe^{2+} or Fe^{3+}). At low pressure, ferric iron is most likely to be four-fold coordinated and acts as a network former, as Al^{3+}, whereas ferrous iron is five to six-fold coordinated and acts as a network modifier (see Mysen, 2006; Mysen and Richet, 2019 and references therein). However, the role of ferrous and ferric iron in melts is still debated as some studies demonstrated that both could be four to six-fold coordinated and therefore they could both act as network modifier (Ghosh and Karki, 2020). Recent study of Ghosh and Karki (2020) displayed indeed that iron redox state has limited impact on the general melt properties. In contrast, the iron spin state has more influence on the structural properties of the melt. Some uncertainties on the behavior of cations in the melt remain and, one of the major unknown so far is the isotopic properties of melts, including those of silicon (^{28}Si, ^{29}Si, ^{30}Si) and iron (^{54}Fe, ^{56}Fe, ^{57}Fe, ^{58}Fe).

Analytical developments and improvements over the past two decades enabled scientists to investigate non-traditional stable isotope fractionation at high-temperature. Several studies carried out on natural and experimental samples have revealed measurable (> 0.05 ‰) silicon and iron isotopic fractionations in igneous systems: i) Iron and silicon display heavy isotope enrichment during magmatic differentiation, although the trends are different (e.g. Weyer et al., 2005; Williams et al., 2005; Poitrasson and Freydier, 2005; Shahar et al., 2008; Schoenberg et al., 2009; Savage et al., 2011; Sossi et al., 2012; Weyer and Seitz, 2012; Dauphas et al., 2014; Zambardi et al., 2014; Foden et al., 2015; Nebel et al., 2015; Poitrasson and Zambardi, 2015; Gajos et al., 2016; Williams et al., 2018; Li et al., 2020), ii) Oceanic crust (MORB and Ocean Island Basalts (OIB)) displays heavier iron isotope signature than some mantle peridotites (e.g. Williams et al., 2009; Williams and Bizimis, 2014; Konter et al., 2016; Sossi et al., 2016; Nebel et al., 2018), iii) There is significant iron isotopes fractionation, associated to Fe-Mg chemical zoning, within single crystals of olivine (Teng et al., 2011; Sio et al., 2013; Oeser et al., 2015; Collinet et al., 2017a; Sio and Dauphas, 2017; Prissel et al., 2018; Sio et al., 2018; Oeser et al., 2018). The potential processes involved in the documented isotopic variations, such as partial melting (e.g. Weyer and Ionov, 2007; Williams et al., 2009; Sossi et al., 2016; Deng et al., 2019), fractional crystallization (e.g. Schuessler et al., 2009; Sossi et al., 2012; Telus et al., 2012; Foden et al., 2015; Du et al., 2017), diffusion-driven kinetic fractionation (Lundstrom, 2009; Zambardi et al., 2014) or even fluid exsolution during late stage of differentiation (Poitrasson and Freydier, 2005; Heimann et al., 2008; Telus et al., 2012), were then investigated. However, interpretations of these observed isotopic variations are often limited by the lack of available equilibrium fractionation factors between coexisting phases, especially between minerals and silicate melts. Hence, the models used in the literature are under-constrained and precise quantification of the processes involved in Fe and Si isotopic fractionation in igneous rocks is hampered. It became then essential to obtain Si and Fe isotope compositions of various melts in order to quantify the processes associated to the isotopic variations in magmatic settings. By now, only few experimental and in-situ studies were carried out to obtain iron isotope composition of melts, using glasses as a proxy. Dauphas et al. (2014) displayed

significant variations in Fe isotope fractionation factors with varying composition of melts. Nevertheless, the mechanisms involved in isotopic fractionation in melts are still under-constrained. The degree of mass-dependent equilibrium fractionation between minerals has been associated to the oxidation state (for Fe; e.g. Polyakov and Mineev, 2000; Dauphas et al., 2014), the bonding environment (i.e. bond length and coordination number; e.g. Sossi and O'Neill, 2017), and the local chemical environments of the atoms of interests (nature and number of the second neighbors; Macris et al., 2015, Rabin et al., 2021). Grant (1954) and Poitrasson and Zambardi (2015) proposed polymerization degree as a key factor influencing the Si isotope fractionation during magmatic differentiation. However, at the mineral scale, this relationship does not seem to be the sole parameter involved (Méheut and Schauble, 2014; Qin et al., 2016; Rabin et al., 2021). The mechanisms listed above could play as well an important role on silicon and iron isotope fractionation in melts.

To investigate the mechanisms involved in melt isotope fractionation, we have calculated consistent Si and Fe β-factors for various melt compositions using first-principles molecular dynamics (FPMD). In this study, five silicic melt compositions were investigated in order to assess the effect of increasing sodium, iron and silicon contents on the Si and Fe isotope composition of melts at 1 GPa. The pressure effect on isotope fractionation is also explored through a FPMD basalt simulation at 12 GPa. Our calculated Si and Fe β-factors for melts were combined to the set of Fe and Si β-factors of silicate and oxide minerals calculated by Rabin et al. (2021) and Qin et al. (2016) to obtain a full set of equilibrium fractionation factors between minerals and melts of various compositions. These data enable us to discuss the impact of equilibrium fractionation, through different processes such as fractional crystallization and partial melting, on Fe and Si isotopes systematics in igneous contexts.

2- METHODOLOGY

2.1- Modelling approach

The structure properties as well as the reduced partition function ratios of each melt were obtained from FPMD simulations based on density functional theory (DFT). All calculations were performed using the Perdew-Burke-Ernzerhof (PBE) parametrized generalized gradient approximation (GGA) functional (Perdew et al., 1996) implemented in the Vienna Ab-initio Simulation Package (VASP; Kresse and Furthmüller, 1996). The interaction between the valence and core electrons were modelled using the projector-augmented wave (PAW) method (Kresse and Joubert, 1999). Plane-wave cutoff of 500 meV and Brillouin-zone sampling at Gamma are used. The simulation cell of each system is constrained to a cube (Table 1). The design of the different melt structures in this study was conducted in 3 steps: i) A primary melt structure including 4 compounds (MgO, CaO, Al_2O_3, SiO_2) was generated using classical molecular dynamics (MD) simulations, for few nanoseconds, based on DL-POLY code (Smith et al., 2002) and using empirical potentials proposed by Matsui (1994). ii) Substitution of some Mg atoms by Fe, some Ca atoms by Na or K was then performed in order to reach the desired melt compositions. iii) The structure thereby created was used as starting composition for the FPMD simulations. The structure was first equilibrated at high temperature (well above the melting point, > 6000 K) using NVT canonical ensemble (fixed number of atoms N, constant volume V and constant temperature T) and then cooled down to a desired lower temperature (4000 K). A temperature of 4000 K was settled in order to preserve the liquid state of the melts during the MD simulations (e.g. Bajgain et al., 2015; Ghosh and Karki, 2018; Caracas et al., 2019). Once the system was at the desired temperature, the isothermal-isobaric ensemble NPT (fixed number of atoms N, constant pressure P and constant temperature T) with variable-cell dynamics was used, for few picoseconds (ps) to optimize the cell parameters of each different melt composition (Table 1). The volume of the melt is indeed a key parameter as the liquid structure is primarily a function of volume, rather than pressure (Karki, 2010). Then, NVT canonical ensembles were used to explore the effect of the various liquid compositions, as well as the pressure effect, on iron and silicon isotopic properties. Both NPT and NVT ensembles used Nosé thermostats (with a Nosé mass-parameter of 3; Nosé, 1984). Each system

contains at least 100 atoms in order to have a simulation cell large enough to calculate equilibrium properties (Karki, 2010). To confirm that 100-atoms simulation cells were sufficient to describe the short- and medium-range properties of the silicate melts, a calculation on a 183-atoms simulation cell was also performed. The duration of the FPMD NVT simulation is also a critical parameter in order to satisfy the ergodicity principles (i.e. the system explores all the possible states of the system, with the same probability as in a liquid, during the simulation time). Therefore, the simulations were carried on for approximately 20 picoseconds in order to acquire representative ensemble at the desired temperature (Bajgain et al., 2015). Analysis of the mean-square displacements (MSD) as a function of time (Allen and Tildesley, 1989) were performed for each temperature-volume-composition condition, in order to confirm that the system stays in the liquid state (Appendix A -Supplementary material, Fig. S1 to S7).

The mean pressure applied during the simulations is chosen to be around 1 GPa (corresponding to a crustal depth of ~35 km), in order to reproduce the pressure conditions of deep magmatic chambers such as in Montagne Pelée (Pichavant, 2002) or Iceland (Kelley and Barton, 2008). Moreover, partial melting happens at pressures between 1 and 3 GPa (e.g. Bertka and Holloway, 1994). The exact mean pressures of each melt are displayed in Table 1 and more detailed analysis of pressure evolution during the MD simulations are available in the Appendix A - Supplementary material, Fig. S8.

The melts simulated here are composed of 7 to 8 chemical elements (Na, Ca, K, Fe, Mg, Al, Si, O) in order to reproduce faithfully natural melt compositions. Three calc-alkaline melts (iron-rich (IR) basalt, iron-depleted (ID) basalt and trachyte), and two peralkaline melts (basanite, phonolite) were studied in order to assess the isotopic evolution of the melt through differentiation (increasing SiO_2 content) as well as the effect of alkaline content in the melts on iron and silicon isotopic fractionation. Rhyolitic melt was not modelled in this study, despite being of high interest as it is expected to display heavier iron isotopes composition than basalt (e.g. Dauphas et al., 2014; Roskosz et al., 2022). The low iron content of such melt would require a simulation cell larger than the ones used here, which is out of our calculation capacity. The melts compositions are displayed in Table 2. Ghosh and Karki (2020) showed that iron spin state configuration is a major parameter that influences greatly (> 15 %) the structural parameters of the melt. In our study, iron atoms are set up in high spin-state because it is known that iron is predominantly in high-spin states in glasses and melts at pressures relevant to crust formation (Mysen and Richet, 2019b and references therein). The Hubbard U term was not added to the DFT calculation as previous studies showed that there are no significant changes in terms of Fe local environment and melts properties (spin and valence state) between GGA and GGA+U calculations in liquid systems where Fe is in high-spin state, especially at high temperature (e.g. Karki et al., 2018; Caracas et al., 2019; Solomatova and Caracas, 2019; Ghosh and Karki, 2020). All iron atoms in the melts were set up as Fe^{2+}, in order to be closer to natural Fe^{3+}/Fe_{tot} composition as MORB displays Fe^{3+}/Fe_{tot} of about 0.09 ± 0.2 (Bézos et al., 2021) and OIB of about 0.2 (Cottrell and Kelley, 2014). The Born-effective charge tensors that represent the first-order response of the atomic positions to an electric field, were obtained for iron through VASP in order to control the valence of iron in each melt simulation.

In addition to melt simulations, first-principles calculations are performed on two silicate minerals (Appendix A - Supplementary material, Table S1), using the same GGA-PBE functional and PAW pseudo-potentials as described above. These silicate minerals, already studied in Rabin et al. (2021), are aegirine ($FeNaSi_2O_6$) and forsterite ($Fe_{0.25}Mg_{1.75}SiO_4$). The only purpose of these calculations is to assess the potential bias related to the use of different pseudo-potentials on the Fe and Si β-factors of silicate minerals. This will allow us to provide a more accurate set of fractionation factors between silicate minerals and melts using mineral data from Rabin et al. (2021).

2.2- Calculation of equilibrium isotope fractionation factors

The equilibrium isotope fractionation factor $\alpha_{(a,b,Y)}$ of an element Y between two phases a and b is defined as:

$$\alpha_{(a,b,Y)} = \frac{\beta_{(a,Y)}}{\beta_{(b,Y)}} \qquad \text{Eq. (1)}$$

where $\beta(a,Y)$, called β-factor, is the reduced partition function ratio between phase *a* and a perfect gas of Y atoms. The usual notation of isotope fractionation, in permil (‰), is written $10^3 \ln\beta\,(a,Y)$. The isotope fractionation factor is therefore expressed as $10^3 \ln\alpha(a,b,Y) = 10^3 \ln\beta\,(a,Y) - 10^3 \ln\beta\,(b,Y) \approx \Delta_{a\text{-}b} = \delta_a - \delta_b$. The notations δ_a and δ_b, used in laboratory studies, represent the isotopic compositions of coexisting phase *a* and *b* and are expressed as, in the case of iron:

$$\delta^{57}Fe\ (‰) = \left(\frac{\left({}^{57}Fe/{}_{54}Fe\right)_{sample}}{\left({}^{57}Fe/{}_{54}Fe\right)_{standard}} - 1 \right) \times 1000 \qquad \text{Eq. (2)}$$

The reduced partition function ratios of the melts were calculated in this study using two different methods referred to as the "snapshot" method and the velocity auto-correlation function, "VAF" method.

2.2.1- The "snapshot" method

The molecular dynamics trajectories are constituted of up to 40 000 time-steps (Δt = 0.5 fs). In order to obtain the β-factor of each melt, a number of snapshots are extracted from the trajectory, at regular time interval, large enough to consider the snapshots as independent from each other. Then, each snapshot structure is relaxed to their equilibrium structure at T = 0 K and a finite pressure of 1 GPa, until the residual forces on atoms are less than 10^{-4} Ry/au, and the residual pressures smaller than 0.002 GPa. Hence, the equilibrated structure does not correspond anymore strictly to a melt but rather to a glass. The "frozen phonon" approach is then used to determine the dynamical matrix for each snapshot: 1) Phonopy code (Togo and Tanaka, 2015) is used to generate the 6N (N = number of atoms in the simulation cell) configurations corresponding to each atomic displacement in the three dimensions (3N in the positive axis, 3N in the negative axis as it is a glass without symmetry). 2) self-consistent field (scf) calculations are then performed on each configuration using VASP. 3) Post-treatment is performed with Phonopy to obtain the dynamical matrix that is subsequently diagonalized for the two atomic masses of interest in order to obtain the vibrational frequencies for both isotopologues. The reduced partition function ratio is finally calculated from these vibrational frequencies (Bigeleisen and Mayer, 1947):

$$\beta(a,Y) = \left[\prod_{i=1}^{3N_{at}} \frac{\nu_i}{\nu'_i} \frac{e^{\left(-\frac{h\nu_i}{2k_bT}\right)}}{1-e^{\left(-\frac{h\nu_i}{k_bT}\right)}} \frac{1-e^{\left(-\frac{h\nu'_i}{k_bT}\right)}}{e^{\left(-\frac{h\nu'_i}{2k_bT}\right)}} \right]^{1/N} \qquad \text{Eq. (3)}$$

where, ν_I and ν'_I are the vibrational frequencies of the two isotopologues (the prime symbol refers to the light isotope of the element *Y)*, identified by a branch index *i* from *1* to $3N_{at}$; N_{at} is the number of atoms in the simulation cell containing *N* atoms of the element *Y*; *h* is the Planck constant, k_b is the Boltzmann constant, and *T* the temperature (in Kelvin). Equation (3) takes into account that there should be no isotopic fractionation at the high-temperature limit (i.e. the "Redlich-Teller" rule, Redlich, 1935).

In order to obtain accurate and precise Si and Fe β-factors for each melt, "frozen phonon" calculations were performed on 6 to 10 snapshots per FPMD simulation. The snapshot β-factors are then averaged in order to obtain a mean β-factor for each melt and the uncertainties associated correspond to the standard error of the mean β-factor. In this method, the interatomic force constant (F) can be calculated from the dynamical matrix by averaging the force constants of the atom of interest (Fe or Si) in the three spatial dimensions *x*,*y*,*z*. The number of snapshots is large enough as shown by the cumulative mean of the β-factor and Fe force constant (Appendix A - Supplementary material, Fig. S9).

The same methodology based on the vibrational frequencies was used to calculate the β-factors of the two minerals, except that only 3N configurations were generated by Phonopy, because of crystal symmetry.

2.2.2 - The "VAF" method

The "snapshot" method described above is a tried-and-tested method, especially for solvated species (Kowalski and Jahn, 2011; Dupuis et al., 2015; Pinilla et al., 2015; Ducher et al., 2018) but the resultant β-factor does not strictly correspond to a liquid but rather to a glass as the atomic positions are relaxed at T = 0 K prior to the calculation of the β-factor. Another approach that allows to keep the temperature effect and the liquid properties (i.e. configurational disorder as well as possible anharmonic effects), is a method based on the kinetic energy of the atoms during the simulations following the thermodynamic perturbation theory (Landau and Lifshitz, 1980) where the β-factor is expressed as:

$$ln\beta_{AX} = \frac{m - m\prime}{m}\left(\frac{K}{RT} - \frac{3}{2}\right) \qquad \text{Eq. (4)}$$

where K is the kinetic energy of the element of interest and can be calculated from the partial vibrational density of state (VDOS) noted *g(e)*:

$$K = \frac{3}{2}\int_0^{e_{max}} E(e/k_BT)\, g(e) de \qquad \text{Eq. (6)}$$

In equation 6, e_{max} is the maximum energy of the vibrational spectrum, and $E(e/k_BT)$ is the Einstein function of the vibrational energy of a single harmonic oscillator at frequency $\nu = e/h$, expressed as:

$$\frac{E(e/k_BT)}{k_BT} = \frac{e/k_BT}{\exp(e/k_BT)} + \frac{e}{2k_BT} \qquad \text{Eq. (7)}$$

Here, the VDOS, g(e), is obtained from the Fourier transform of the velocity auto-correlation function (VAF) thermodynamically averaged over all atoms (Meyer and Comtesse, 2011):

$$g(e) = \int_{-\infty}^{\infty} dt\, \frac{\sum_{i=1}^{N}\langle V_i(t)|V_i(0)\rangle}{\sum_{i=1}^{N}\langle V_i(0)|V_i(0)\rangle}\, e^{i2\pi\nu t} \qquad \text{Eq. (8)}$$

where V_i is the velocity of the i-th atom.

In this method, the interatomic force constant can also be retrieved from the VDOS, using the following equation (e.g. Dauphas et al., 2012) :

$$\langle F\rangle = \frac{m}{\hbar^2}\int_0^{+\infty} g(e)\, e^2 de \qquad \text{Eq. (9)}$$

In this study, the "VAF" method is applied on 10 000 time-steps trajectories (5 ps), enabling us to obtain 2 to 4 β-factors for each melt that are then averaged. Uncertainties are estimated as the 2-standard

error of this calculated mean. The "VAF" method was only applied on iron isotopes as iron can be a network modifier, more likely to be affected by the transition liquid-glass (i.e. Fe-O coordination number, Fe-O distance) compared to Si that is a network former.

The main limitation of using the VDOS to calculate the β-factor of a liquid is the fact that the VDOS display a non-zero value at zero frequency due to diffusion effects. In principle, this diffusive contribution should be removed before calculating the β-factor. Such corrections in complex silicate melts would be difficult to achieve since it would require precise knowledge of the molar volume contribution of each species in the melt. Furthermore, Pinilla et al. (2021) showed that these fluidicity effects were negligible in the calculation of equilibrium fractionation factor of iron in liquid $Fe_{x-1}S_x$ alloys. Therefore, such effects were neglected here.

3- RESULTS

3.1- Structural melt properties

The partial radial distribution functions (RDF) of the different atomic species pairs present in the silicate melts were analyzed in order to determine the average interatomic distances as well as the atomic coordination (Appendix A - Supplementary material, Fig. S10 to S16). The atomic coordination (C) for a given species A with respect to another species B can be expressed as:

$$C_{AB} = 4\pi\rho_B \int_0^{r_{min}} r^2 g_{AB}(r) dr \qquad \text{Eq. (9)}$$

where $g_{AB}(r)$ is the partial radial distribution function of the A-B atomic pairs and C_{AB} represents the number of atoms of species B which lie within a spherical region of radius r_{min} centered around the atom of species A.

The average cation-oxygen distances and CN are displayed in Table 3 and the results are described in Appendix A - Supplementary material (under the heading "The structural properties of the melt"). The results are generally consistent with previous molecular dynamics results performed at high temperature (e.g. Guillot and Sator, 2007a; Bajgain et al., 2015; Ghosh and Karki, 2018; Caracas et al., 2019; Ghosh and Karki, 2020; Feng et al., 2021; Solomatova and Caracas, 2021). The 183-atoms simulation of the basalt_IR displays similar cation-oxygen coordination numbers (difference < 1.8%) and cation-oxygen average bond lengths (difference < 1%) as the 100-atoms simulation (Table 3). This allows us to confirm that 100-atoms simulations are large enough to discuss about the short- and medium-range structural properties and therefore equilibrium isotopic properties.

Detailed analyses of iron and silicon environment in the different melts were performed by calculating the average distance between Fe or Si and their first cation neighbors as well as the corresponding coordination numbers (Table 4). The iron cationic neighbors are at a distance > 2.9 Å for all elements and all melts, except in iron-rich melts where the average distance between two iron atoms can be as low as 2.25 Å. Silicon is the most represented neighbor with an average Fe-Si coordination number between 3.02 and 4.30. The other elements display a Fe-cation coordination number < 2, except for Fe-Al coordination number in the phonolite (3.09). The silicon cationic neighbors are at a distance > 3 Å for all elements and all melts. The silicon close environment is more varied, with no clear preference in term of nature of second neighbors (Si, Al, K). The average number of network formers (Si+Al) around Si are always > 3.8 except for basalt_ID that has an average number of 1.87. This would suggest that iron-depleted basalts (basalt_ID), unlike the other melts, cannot form a proper tetrahedral network. This agrees with Guillot and Sator (2007a) conclusions.

The degree of polymerization is an important parameter that is directly associated to the composition of the silicate melts. According to Mysen et al. (1985), a melt can be described in term of degree of polymerization, designated as NBO/T where NBO represents the number of Non-Bridging Oxygen atoms, and T stands for Tetrahedrally coordinated cations representing the network formers (Si and Al in this study). These NBO/T ratios (Table 2) show that the more evolved melts such as trachyte and phonolite (NBO/T = 0.28) are more polymerized than the basaltic melts (NBO/T=1).

The structural homogeneity of melts can be defined according to glass specialists using a simple parameter characterizing the degree of occupation of the interstitial site C=M/T (Kuryaeva, 2004), where M represents the network- modifiers, and T the network formers. A melt structure is considered homogeneous when C < 0.27. The melt heterogeneity is mostly driven by the total concentration of alkali and alkali-earth metals oxides (Kuryaeva, 2004). In this study, melts are heterogeneous, displaying C values ranging between 0.45 for phonolite and 0.67 for the calc-alkaline basalt_IR and basalt_ID. This high degree of occupation of interstices is indeed favorable to individual structural groupings in the melts (i.e. microheterogeneous structure). The heterogeneity of aluminosilicate melts, caused by high content of sodium cations, leads to changes in the properties that are not accounted for in the degree of polymerization calculation. This explains why there is no apparent relationship between NBO/T and the Fe-O coordination number and unclear correlation with Si-O coordination number (Appendix A - Supplementary material, Fig. S17).

3.2. Reduced partition function ratios of iron and silicon

The theoretical reduced partition function ratios have been calculated for iron and silicon. Their temperature dependences are displayed in Fig. 2 as well as their corresponding polynomial fits in Table 5. As observed for minerals (Blanchard et al., 2017; Rabin et al. 2021), there is a linear correlation between melt β-factor and their associated average interatomic force constant (Fig. 3). At 1000 K, the $10^3\ln\beta$ $^{57}Fe/^{54}Fe$ for all melts span in a range of ~ 1.1 ‰ and the $10^3\ln\beta$ $^{30}Si/^{28}Si$ are within a range of ~ 0.5 ‰ (Fig. 2). The variation of Fe isotope compositions within melts are greater than the one observed in silicate minerals whereas the variation of Si isotope compositions is twice larger in minerals relative to melts (Compare Fig. 2 with Fig. 1 of Rabin et al., 2021). Phonolite, the most evolved peralkaline melt displays the highest iron β-factors followed by the calc-alkaline iron-rich basalt (Basalt_IR) whereas the calc-alkaline iron-poor basalt (Basalt_ID) displays the lowest iron β-factors. On the other hand, the highest Si β-factor is found in trachyte, followed closely by phonolite.

3.2.1. "Snapshot" vs "VAF" method.

The Fe reduced partition function ratios were calculated using two methods: the "VAF" method and the "snapshot" method (See Part 2.2). In the "snapshot" method the β-factors are extrapolated to magmatic temperatures using Eq. (3) using the vibrational frequencies calculated at 0 K and P = 1 GPa. On the other hand, β-factors determined by the "VAF" method are extrapolated from the MD run at 4000 K and P $\simeq$ 1 GPa using Eq. (4). Results show that the "VAF" and "snapshot" methods give similar force constants within uncertainties (Table 6) and therefore β-factors since both quantities are linearly correlated (Fig. 3). This is consistent with the fact that the structures obtained with the "snapshot" method are really similar to the ones from the "VAF" trajectories in terms of bond lengths, coordination number and nature of Fe neighbors. The calculated uncertainties are twice larger with the "VAF" method than using the "snapshot" methods, but uncertainties could be certainly reduced by increasing significantly the duration of the simulations. Concerning phonolite, the discrepancy of force constant between the "VAF" and "snapshot" methods associated to extremely large uncertainties, notably for the former method, make the use of these results more difficult. It is clear that phonolite tends to have heavier Fe isotopic values than the other melts. However, the Fe force constant cannot be clearly quantified. This may be caused by the model itself of the phonolite melt that contains only one Fe atom over the 102-atoms system which reduces significantly statistical

sampling. However, outside this exception, the similar Fe β-factors obtained by the "VAF" and the "snapshot" methods allow to conclude that both methods are relevant to determine the isotopic properties of a melt. This conclusion was previously reached by Pinilla et al. (2021) in the case of Fe-S alloys at high pressure and temperature conditions. This also means that potential anharmonic effects, that are at least partially taken in account with the "VAF" method, are negligible considering the uncertainties obtained and that extrapolation of Fe β-factors at high temperature from force constants obtained at low temperature is relevant (e.g. NRIXS and Lamb-Mössbauer measurements; Dauphas et al., 2014; Roskosz et al., 2022). In the discussion and applications parts, the only results that will be considered are the ones obtained from the "snapshot" method for clarity and consistency with Si isotopes results.

3.2.2 – Fractionation factors between minerals and melts.

One of the major issues in determining the processes involved in iron and silicon isotope fractionation during magmatic differentiation is the lack of equilibrium Fe and Si fractionation factors between minerals present at magmatic temperatures (i.e. pyroxene, olivine, oxides...) and their associated melts. In this study, we combine the Fe and Si β-factors of various minerals present in magmatic setting, obtained from first-principles calculation (Rabin et al. 2021) with the present iron and silicon β-factors of the melts in order to obtain a full set of equilibrium fractionation factors between minerals and melts ($\Delta^{57}Fe_{mineral\text{-}melt}$ and $\Delta^{30}Si_{mineral\text{-}melt}$). The entire set of Fe and Si equilibrium fractionation factors between minerals and melts, calculated after systematic bias correction (Appendix B- Supplementary Data), is displayed in Table 7.

It is noticeable that most of the minerals display lighter iron and silicon isotope composition than the different melts at equilibrium (Appendix B - Supplementary material). Only albite, anorthite, quartz and fayalite that display heavier silicon isotopic relative to the different melts. Likewise, aegirine and magnetite display heavier iron isotopic signature than basalt_ID, basanite and trachyte melts. As expected, fayalite, with its low iron force constant (F = 100 N/m), is the mineral that shows the greatest iron isotope fractionation with the different melts, followed by aegirine, hedenbergite and augite (Appendix B - Supplementary material).

4- DISCUSSION

4.1 – Iron and silicon environment in the silicate melts.

Our results on the iron and silicon structural properties allow us to discuss the iron and silicon environment in the different investigated melt. As mentioned in part 3.1, silicon structural properties are independent of the melt composition whereas iron is sensitive to the compositional change of the melt.

The nature of the network former in the melt is one of the parameters investigated that have an impact on iron atoms bonding-properties. We observe a linear relationship between Fe-O coordination number and the Al/(Si+Al) ratio in melts as described in previous studies (Mysen et al., 2003). Phonolite and basanite display the highest Fe-O coordination numbers that correspond to the highest Al/(Si+Al) ratio. Peralkaline undersaturated melts are indeed, by definition, depleted in silicon. The increasing aluminum content as network former over silicon results in an increase of the coordination number of all the network modifiers (Table 3) including the part of aluminum acting as network modifier (Fig. 1).

The iron effective charge in the investigated melts shows little variation (2.28-2.37) that cannot be correlated to systematic changes in coordination number or Fe-O distances (Tables 2 and 3). This

agrees with the study of Ghosh and Karki (2020) showing that ferric and ferrous iron can have the same coordination number in melts and that variations of iron effective charge in melts cause no significant change of the structural properties of iron.

The structural heterogeneity of the melts, defined in part 3.1 as related to the abundance of network modifiers, indicates the potential presence of individual structural groupings that could also induce segregation of cations in the melts. Therefore, it is interesting to look at the nature and distribution of the network modifier cations around iron and silicon (Table 4). Iron tends to favor iron as its closest neighbor in melts when iron concentration is relatively high (basalt_IR, basanite; Table 4). The distribution of iron atoms as a next nearest neighbor (NNN) of another iron can be determined by dividing the number of Fe NNN by the total number of its NNN's (i.e. $CN_{Fe\text{-}Fe}/CN_{Fe\text{-}X}$, with X = Fe, Ca, Na, Si, Mg, and Al, Rossano et al., 2000). In the case of a random distribution of cations in the melt structure, this ratio is only dependent of the melt stoichiometry. For the basaltic melt (basalt_IR), a random cation distribution model predicts a value of 0.1, while our FPMD simulation indicates a value of 0.14. Concerning the basanite melt, a random distribution of iron in the melt corresponds to a value of 0.12. FPMD basanite simulation gives a ratio of 0.14. These results suggest a slight segregation of iron in the basanite and basalt_IR melts. Concerning silicon, unlike iron there is no systematic preferences in term of the nature of second neighbors. The next nearest neighbor of silicon is alternatively silicon itself, aluminum, potassium or even calcium.

4.2 – Silicate glasses vs silicate melts.

In many experimental studies, glasses are the only proxy for melts. When the melt quenching is fast enough to avoid cation reorganization, then the glass structure associated is most likely to be close to the melt one as observed with the snapshot method. A comparative study of MD simulation and experimental glasses shows that cation-oxygen distances are slightly larger in glasses than in melts even if the structure properties are very similar (Rossano et al., 2000). Feng et al. (2021) exhibited notable structural changes (i.e. density) between the basaltic glass and its molten counterparts, especially at low pressure. Ghosh et al. (2021) also pointed out that the effects of temperature on the Fe-O coordination is not negligible, with a silicate glass at 300 K displaying Fe-O coordination of 4.5 whereas melt at 3000 K have a Fe-O coordination of 3.7. In the case of isotopic variation between melts and glasses, this question has not really been assessed. As stated in the methods section, the "VAF" method takes into account all features of the melt system whereas the "snapshot" method involves a relaxation of atomic positions at zero temperature. Both methods give similar β-factors. However, it is noteworthy that this computational structural relaxation does not mimic exactly the quench of a glass that is inevitably slower. Many studies observed that the coordination number of an element is a parameter that will affect its isotopic signature in a material (e.g. Polyakov and Mineev, 2000; Méheut et al., 2009; Sossi and O'Neill, 2017; Rabin et al., 2021). Therefore, it is possible that silicate glasses are not an ideal proxy for melts, as glasses display significantly higher coordination numbers and therefore will underestimate the melts β-factor.

4.3 – Iron isotope fractionation in melts.

4.3.1 – Parameters controlling Fe isotope fractionation.

In silicate minerals, the main parameters involved in iron isotope fractionation, besides temperature, are the oxidation state of iron, i.e. Fe^{3+}/Fe_{tot} (Polyakov and Mineev, 2000; Shahar et al., 2008; Dauphas et al., 2014), the Fe-O bond length, the Fe-O coordination number (Sossi and O'Neill, 2017) and the number and nature of iron second-neighbors (Macris et al., 2015; Rabin et al., 2021). All these parameters are also expected to have an impact on melt iron isotope composition. However, the

importance of a parameter over another can change due to the structural differences between melts and minerals. Furthermore, the range of Fe β-factors within those melts is greater than what was observed in silicate minerals (Compare Fig. 2 with Fig. 1 of Rabin et al., 2021).

The first important observation from these FPMD simulations is that the variations in Fe-O coordination number (from 3.7 to 4.7) does not seem to be correlated to the iron force constants (Fig. 4a). Trachyte that has a Fe-O coordination number of 3.74, displays a similar force constant <F> (191 ± 20 N/m) as basanite (196 ± 13 N/m) that has a Fe-O coordination number of 4.73. The second main observation is the iron force constant dependency on Fe-O distances (Fig. 5a). The basalt_IR has the highest Fe force constant (243 ± 17 N/m) associated to the shorter Fe-O bond length (1.76 Å). This is consistent with the study of Sossi and O'Neill (2017) that shows that the silicate minerals with the shorter Fe-O bonds tend to be enriched in heavy ^{57}Fe.

Dauphas et al. (2014), revised by Roskosz et al. (2022), demonstrated that there is a relationship between iron force constant and Fe^{3+}/Fe_{tot} in silicate glasses produced under different level of oxygen fugacity (Fig. 6) with the glasses synthetized under high oxidizing condition displaying the highest Fe force constant. They also demonstrated that Fe^{2+}-glasses ($\log(fO_2) = -8$) have large variations of iron force constant (from 188 ± 7 up to 251 ± 10 N/m) depending on their SiO_2 content. This range is relatively similar to the one observed in our study (from 171 ± 8 up to 243 ± 17 N/m), however no relationship between SiO_2 content and force constant is observed in our study given the silica range investigated (Fig. 6). In addition, Roskosz et al. (2022) also displayed iron mean force constant variations in Fe^{2+}-rich melts with similar SiO_2 content. Therefore, the variation of Fe force constant in melts with similar Fe^{2+} and SiO_2 content definitely means that iron isotope fractionation within silicate melts cannot be uniquely explained in term of iron redox state or network-former concentration.

In addition to the lack of relationship between Fe force constant and SiO_2 content, there seems to be no correlation between iron force constant and the melt polymerization parameter NBO/T (Fig. 7a). However, there is a relationship between the Fe-Fe and Fe-Mg distances and iron force constants: a decrease of these distances leads to higher iron force constant (Fig. 8c and d). This explains why basalt_IR and basanite display higher force constant than the basalt_ID and trachyte (Table 6). This suggests that, like for minerals (Macris et al., 2015; Rabin et al., 2021), the melts iron force constant could be influenced by the Fe local environment. However, there is no clear relationship between iron/magnesium concentration in the melts and the iron force constant (Fig. 9). Further investigations are necessary to confirm and quantify the impact of the Fe local environment on the iron force constant. Sodium cations might also play a role on iron isotope fractionation in melts even if there is no direct relationship between Fe-Na distances or Na_2O and iron force constant (Figs. 8, 9). As discussed in part 3.1.2, the content of sodium drives the structural heterogeneity of the melt, enabling the observed segregation of cations around iron atoms. Roskosz et al. (2022) also suggested that melts composition and more precisely the presence of K or Na cations leads to higher force constant. Here, we do not observe a higher force constant in the trachytic melt where the concentration of K and Na is relatively high. The major difference between this study and the one by Roskosz et al. (2022) is that they used simplified melt compositions, therefore the variety of the iron second neighbors was narrowed (Na or K and Fe itself). Furthermore, we display in the present study that neither Na nor K cations are favored as Fe second neighbor in a natural-like melt where the composition is more complex, except the highly alkaline melt (i.e. phonolite). Overall, our theoretical study agrees with Roskosz et al. (2022) on the fact the nature of the cations in the melts, and most likely the nature of the cations surrounding Fe atoms, seems to affect the iron force constant.

Hence, Fe isotope fractionation in melts appears mainly driven by the Fe-O bond length and by the nature and number of the network-modifier cations around iron atoms.

4.3.2 - Comparison between theoretical and experimental data

Dauphas et al. (2014) were the first to provide experimental iron β-factors of silicate terrestrial glasses of various compositions, as proxy of melts, using Nuclear Resonant Inelastic X-ray Scattering (NRIXS). In Fig. 6, iron force constant obtained by NRIXS (Dauphas et al., 2014) are compiled with our calculated ones. The range of iron force constants of their Fe^{2+}-basaltic glasses (from 197 ± 8 N/m up to 292 ± 18 N/m) are similar to our calculated iron force constants for Fe^{2+}-basaltic melts at 1 GPa (between 171 ± 8 N/m up to 243 ± 17 N/m), although their major element compositions are different. For the most evolved lavas, our trachyte iron force constant is consistent with that of Dauphas et al. (2014). They found no major increase in the iron force constant until late stage of magmatic differentiation (~ 70 wt% of SiO_2) for the silica-saturated series. No measurement on silica undersaturated peralkaline glasses were performed which prevents us to compare our phonolite and basanite iron β-factor. Later, Prissel et al. (2018) determined iron force constants between 189 ± 9 and 203 ± 11 N/m for their synthetic lunar glasses using NRIXS that is undistinguishable from Dauphas et al. (2014) estimates for terrestrial basalts under IW fO_2 conditions (See Fig. 4 of Prissel et al., 2018) and lies within our range of values for terrestrial basalts. Dauphas et al. (2014) and Prissel et al. (2018) concluded at no Fe isotope fractionation between forsterite and melts of various planetary composition, including terrestrial since they have the same force constant. Our calculated fractionation factor between forsterite and the basalt with low iron content (Basalt_ID) $\Delta^{57}Fe_{forsterite\text{-}basalt\_ID}$ = -0.01 ‰ at 1500 K agrees with such a conclusion. However, this study displays a fractionation factor between forsterite and the basalt with high iron content (FeO = 13.1 wt%) $\Delta^{57}Fe_{forsterite\text{-}basalt\_IR}$ = -0.15 ‰ at 1500K. If the range of Fe force constant calculated for the melts is similar to the measured one for glasses (Prissel et al. 2018, Dauphas et al. 2014), our basaltic melt with high FeO content displays higher iron force constant than the basalt with elevated FeO contents investigated by Prissel et al. (2018). As we underlined in part 4.3.1, multiple parameters tend to affect the iron force constant of the melts, including differences of compositions (e.g., the addition of titanium in the glasses studied by Prissel et al. (2018), although these authors did not see an effect on the Fe force constant). Also, our calculation does not take into account the possible effect of variable melt fO_2 (Part 2.1). Moreover, our forsterite Fe force constant calculated by DFT (162 ± 8 N/m) is also lower than the one obtained by NRIXS measurements (197 ± 10 N/m; Dauphas et al. 2014).

Other studies mainly focused on inter-mineral iron isotope fractionations (Polyakov and Mineev, 2000; Shahar et al., 2008; Dauphas et al., 2012; Macris et al., 2015; Roskosz et al., 2015; Sossi and O'Neill, 2017) as measuring iron isotope composition of glasses in equilibrium with minerals is a great analytical challenge on natural and experimental samples. This is why there is only few data on iron isotope fractionation factor between silicate melts and minerals. However, $\Delta^{57}Fe_{mineral\text{-}melt}$ were assessed empirically in many studies performed on natural samples in order to model fractional crystallization and other related processes (e.g. Sossi et al., 2012; Sossi et al., 2016; Williams et al., 2018). Williams et al. (2018) determined a $\Delta^{57}Fe_{melt\text{-}cpx}$ of 0.15 ‰, based on the observed difference in mean Fe isotope composition between oceanic basalts and fertile mantle peridotites (Williams and Bizimis, 2014) with no indication of the temperature dependence. Assuming a temperature of 1000 K, our calculated $\Delta^{57}Fe_{Basalt\_ID\text{-}Augite}$ and $\Delta^{57}Fe_{Basalt\_ID\text{-}Hedenbergite}$ of about 0.12 ‰ as well as $\Delta^{57}Fe_{Basalt\_ID\text{-}Diopside}$ = 0.08 ‰ are only slightly lower than the empirically determined one. However, looking at iron-rich basalt, our calculated $\Delta^{57}Fe_{Basalt\_IR\text{-}Augite}$ and $\Delta^{57}Fe_{Basalt\_IR\text{-}Hedenbergite}$ of about 0.42 ‰ as well as our $\Delta^{57}Fe_{Basalt\_ID\text{-}Diopside}$ = 0.38 ‰ appear significantly larger than the 0.15 ‰ value proposed by Williams et al. (2018). Depending on the iron content in the melt $\Delta^{57}Fe_{cpx\text{-}melt}$ can vary between 0.08 ‰ up to 0.42 ‰ at 1000 K. This is why strong cautions need to be applied when using $\Delta^{57}Fe_{melt\text{-}mineral}$ to model iron isotope composition of natural samples. It is important to know the exact chemistry of the bulk rock and of the minerals, along with the melt fO_2 (see Fig. 6 and Dauphas et al., 2014; Prissel et al., 2018). The $\Delta^{57}Fe_{melt\text{-}cpx} = 0.25 \times 10^6/T^2$ used by Sossi et al., (2012) to model fractional crystallization at Red hill volcano also fits in the calculated range. Our calculated $\Delta^{57}Fe_{forsterite\text{-}basalt\_IR}$ = -0.15 ‰ at 1500 K agrees with the $\Delta^{57}Fe_{ol\text{-}melt}$ of -0.15 ‰ observed by Teng et al. (2008) at magmatic temperature. However, subsequent in situ Fe isotope measurements from the same group showed that this was essentially a

kinetic effect occurring upon magma cooling (see review in Dauphas et al. (2017)). Hence, this comparison with the literature suggest that our calculated values seem to be on the higher end relative to previous field-based and experimental studies (Williams et al., 2018; Prissel et al., 2018) and further investigations will be needed to clarify why.

4.4 – Silicon isotope fractionation in melts.

4.4.1 – Parameters controlling Si isotope fractionation.

The parameters proposed to control silicon isotope fractionation in silicate minerals are Si-O bond lengths, Si-O polyhedron volume (Qin et al., 2016), Si-O coordination number (Méheut et al., 2009; Méheut and Schauble, 2014; Qin et al., 2016), the nature of silicon second neighbors (Rabin et al.,2021), the electronegativity of the surrounding cations (Méheut and Schauble, 2014), and the polymerization degree (Grant, 1954; Poitrasson and Zambardi, 2015) .

Looking at the melts investigated here, we find that the range of Si isotope β-factors in melts is relatively similar to that observed in silicate minerals, though to the higher end (Fig. 3b), except for fayalite that displays a significantly lower β-factor. The average Si-O bond length and coordination number are similar in all the investigated melts (Table 3). This means that neither Si-O bond length nor Si-O coordination number are responsible for the Si β-factor variation observed in these melts (Fig.4b and Fig. 5b). This lack of relationship between those parameters and the silicon isotope fractionation were also observed in the silicate minerals investigated in Rabin et al. (2021) that all display a coordination of 4, and an average Si-O bond length of 1.65 Å.

The melt polymerization has been proposed to be the main factor causing silicon isotope fractionation among bulk igneous rock series (Poitrasson and Zambardi, 2015). At the mineral scale however, polymerization of SiO_4^{4-} tetrahedra did not appear to be the sole parameter influencing Si isotope fractionation in silicates (Méheut et al., 2009; Méheut and Schauble, 2014; Qin et al., 2016; Rabin et al., 2021). In this study, there seems to be a correlation between NBO/T and Si force constant from basalt to trachyte, considering the associated uncertainties (Fig. 7b). However, Phonolite has a Si force constant of 700 ± 15 N/m associated with a NBO/T ratio of 0.28 whereas basalt_ID has a similar Si force constant (695 ± 13 N/m) but a NBO/T ratio of 1 (Fig. 7b). As underlined part 3.1, variable melts composition, generating structural heterogeneities, can blur the potential correlation with the polymerization parameter NBO/T. This scatter is well observed among terrestrial igneous rocks, as opposed to lunar ones with a simpler petrogenetic history, notably in terms of protolith that were likely less varied on the Moon (Poitrasson and Zambardi, 2015). This suggests that in melts displaying structural heterogeneities, the polymerization degree might not the main parameter influencing silicon isotope composition.

A limited increase in Si force constants with increasing SiO_2 content, a proxy for magmatic differentiation, can also be inferred (Fig. 10). However, there is no relationship between Si force constant and Si-Si distance (Fig. 11), nor with coordination number. The variation of SiO_2 content (from 49.1 to 63.2 wt%) in our simulated melts is relatively reduced. To evidence any strong relationship between Si force constant and SiO_2 content a melt with > 70 wt% silica content would need to be modeled. Silicon force constants are really similar for basalt_ID, basanite and phonolite, with values of 695 ± 13, 687 ± 8 and 700 ± 15 N/m respectively. This means that increasing alkaline and aluminum content in the melts, that seems to play a role on iron isotope fractionation, has no effect on silicon fractionation (Fig. 10). This also demonstrates that electronegativity differences of the cations constituting the melt (χ_{Na} = 0.93; χ_{Mg} = 1.31; χ_{Al} = 1.63) does not affect the silicon isotope composition of the melts. Silicon is indeed a network former in the melts and silicon structural properties as well as the Si force constant are much less sensitive to melt composition than iron. The only significant

variation of Si force constant is between basalt_IR and trachyte with values of 669 ± 11 N/m and 716 ± 10 N/m, respectively. Besides the polymerization degree (Fig. 7b), it seems that the major difference between these two melts are the Si-Fe average distance, of about 3.1 Å for basalt_IR and 2.4 Å for trachyte (Table 4). The shortest average Si-Fe distance corresponds to the highest Si force constant in the melts (Fig. 11).

To conclude, the small but significant silicon isotope fractionation in the melts seems to be mainly driven by either the presence of iron as silicon second neighbors and/or the melt polymerization degree. The nature of the melt, whether peralkaline or calk-alkaline, is not influencing the silicon isotope signature. Further studies with a larger range of SiO_2 content would need to be performed in order to assess whether SiO_2 content is affecting or not the Si isotope composition of the melts.

4.4.2 - Comparison between theoretical and experimental data

As for iron isotopes, most studies focused on inter-mineral silicon isotope fractionation (Méheut et al., 2009; Savage et al., 2011; Méheut and Schauble, 2014; Qin et al., 2016) and there are only two studies reporting so far $\Delta_{melt\text{-}mineral}\ ^{30}Si/^{28}Si$. Qin et al. (2016) and Deng et al. (2019), used the silicon β-factors of silicate minerals calculated by Qin et al. (2016) in order to assess Si fractionation factors between silicate minerals and different melt compositions. These calculations were performed assuming that silicate melts have Si isotope fractionation factors equal to the weighted sum of those for their normative mineral compositions. Our set of Si isotope fractionation factors as well as the one calculated by Deng et al. (2019) at 1123 K are displayed in Figure 12 (and Table S1 – Appendix B – Supplementary material). Both studies display a similar order for Si fractionation factors with $\Delta_{melt\text{-}diopside}\ ^{30}Si/^{28}Si > \Delta_{melt\text{-}orthoenstatite}\ ^{30}Si/^{28}Si > \Delta_{melt\text{-}olivine}\ ^{30}Si/^{28}Si > \Delta_{melt\text{-}anorthite}\ ^{30}Si/^{28}Si > \Delta_{melt\text{-}albite}\ ^{30}Si/^{28}Si$. The silicon fractionation factors calculated by Qin et al. (2016) and Deng et al. (2019) are, however, systematically higher than our calculated $\Delta_{melt\text{-}mineral}\ ^{30}Si/^{28}Si$, by 0.1-0.2 ‰ for the trachytic melt and by 0.4-0.5 ‰ for basaltic (IR) melt. The discrepancies between our calculated silicon fractionation factor between minerals and trachytic melt and the one estimated from Qin et al. (2016) lies within our estimated uncertainties of ≃ 0.3 ‰ at 1123 K. Concerning the basaltic melt, the $\Delta_{mineral\text{-}melt}\ ^{30}Si/^{28}Si$ of Qin et al. (2016) is slightly higher than our calculated $\Delta_{mineral\text{-}melt}\ ^{30}Si/^{28}Si$ within uncertainties. As a result, Qin et al. (2016) would suggest that olivine and enstatite have a lighter silicon isotope composition than the basaltic melts and that the silicon fractionation factor between the feldspars and the melt is insignificant which is not what is observed in our study (Figure 12). The high Si β-factor of the basaltic melt estimated by Qin et al. (2016) and Deng et al. (2019) is probably due to the high content of feldspars in the composition of the magmatic rocks, mainly in the mesostasis. As a consequence, estimated $10^3 ln\beta_{melt}$ is mainly driven by anorthite and albite Si β-factors. From our results, it appears that the melt Si β-factor can hardly be assessed by using the weighted sum of the mineral composition of the melt and their associated Si β-factor, especially for the more mafic ones.

5- APPLICATIONS

5.1 – Magmatic differentiation

5.1.1- Iron isotopes

Iron isotope fractionation has been widely studied on natural samples in the context of magmatic differentiation. Most of the magmatic series display heavy iron isotope compositions in the most evolved lavas (e.g. Teng et al., 2008; Sossi et al., 2012; Williams et al., 2018), especially with SiO_2 content > 70 wt% (e.g. Poitrasson and Freydier, 2005; Schuessler et al., 2009; Zambardi et al., 2014). One of the candidates to explain such isotopic signature is fractional crystallization. However, the impact of fractional crystallization on iron isotope fractionation is still debated. Many studies considered that there is no significant iron isotopic fractionation between Fe^{2+}-minerals and the

associated melt and that magnetite, an Fe^{3+} oxide, is the main mineral phase driving the iron isotope composition in the lavas. Hence, the evolved lavas should display lighter iron isotopic composition (Shahar et al., 2008). Therefore, fractional crystallization has been discarded as potential candidate to explain the observed heavy iron isotope signature at the last stage of magmatic differentiation (Zambardi et al., 2014). However, Dauphas et al. (2014) displayed the first experimental β-factors for glasses (see section 4.3.2 above) and demonstrated that the heavy isotope signature of evolved melts could compensate for the magnetite crystallization during magmatic differentiation. Thus, fractional crystallization could lead to the heavy δ^{57}Fe observed. Besides, Polyakov and Mineev (2000) and Rabin et al. (2021) showed that isotopic fractionation between Fe^{2+}-bearing minerals are significant. Taking this into account in fractional crystallization models could reproduce the isotopic trend observed in natural lavas (Rabin et al. 2021). Here, the model produced in Rabin et al. (2021) was modified by replacing the approximated $\Delta^{57}Fe_{min\text{-}melt}$ (using melt β-factor of Dauphas et al. (2014)), by the $\Delta^{57}Fe_{min\text{-}trachyte}$ calculated in this study (Table 7, Appendix C - Supplementary material -Table E1). Our model shows a smooth increase of δ^{57}Fe from 58 wt% SiO_2 to 74 wt% SiO_2 followed by a sharp increase up to 0.65‰ (Fig. 13a). This sharp δ^{57}Fe increase observed at 74wt% SiO_2 is related to the end of ulvöspinel and magnetite and beginning of ilmenite crystallization (see Appendix C - Supplementary material). If most of the Fe isotope signatures of the evolved lavas and granites (e.g. Poitrasson and Freydier, 2005; Telus et al., 2012; Foden et al., 2015) can be explained by our fractional crystallization model, some of the heaviest iron isotopic signatures observed in some granites (δ^{57}Fe = + 0.9 ‰; e.g. He et al., 2017; Xia et al., 2017) are however not reproduced by this model. Despite the fact that this is the most constrained fractional crystallization model produced so far, the lack of calculated β-factor for rhyolitic melt could under-estimate the δ^{57}Fe of the most evolved melt as rhyolitic melt should have a higher β-factor than trachyte (Dauphas et al., 2014). Overall, from this new model, it is possible to conclude that fractional crystallization may explain at least part of the iron isotope evolution during magmatic differentiation for δ^{57}Fe values up to 0.65 ‰.

5.1.2-- Silicon isotopes

Silicon isotopes show progressive and systematic enrichment in heavy isotopes during magmatic differentiation (Savage et al., 2011; Zambardi et al., 2014) going from δ^{30}Si = -0.30±0.05 ‰ for SiO_2 = 47 wt% up to -0.10±0.07 ‰ for SiO_2 = 76 wt% in terrestrial volcanic rocks. Savage et al. (2011) proposed fractional crystallization as the main process involved in silicon isotope fractionation during magmatic differentiation. However, modelling of the effect of fractional crystallization on δ^{30}Si along magmatic differentiation performed by Savage et al. (2011) and Zambardi et al. (2014), diverge from the measured silicon isotopic trends (Fig. 13b). This discrepancy can be due to the fact that, besides the effect of magma differentiation, igneous rocks silicon isotope composition also records source signatures, such as a possible heavy seafloor chert contribution for andesites and a light clay contribution for anatectic leucogranites (Poitrasson and Zambardi, 2015). Also, the lack of precise fractionation factor between silicate minerals and melt is a limitation for fractional crystallization modeling. Many studies (Méheut et al., 2009; Méheut and Schauble, 2014; Qin et al., 2016; Rabin et al., 2021) underlined that silicon isotope fractionation between silicate minerals, even at high temperature, are significant. The use of approximated $\Delta^{30}Si_{min\text{-}melt}$ allowed Qin et al. (2016) to show, through different models, that fractional crystallization is a viable mechanism to explain heavy silicon isotope signatures in the most evolved lavas. Here, we are modelling the effect of fractional crystallization on silicon isotopes using our $\Delta^{30}Si_{min\text{-}trachyte}$ in order to evaluate this hypothesis (Appendix C - Supplementary material - Table E2). We used the same starting composition in the MCS software as in the model of fractional crystallization for iron isotopes. In this model, silicon isotope evolution is expressed as follow:

$$\delta^{30}Si\ (melt)_{j+1} = \delta^{30}Si\ (melt)_j + \sum_i X_i \times 10^3 \ln \alpha_i\ (T) \qquad \text{Eq. (10)}$$

where X_i is the modal proportion of minerals crystallized at each 5°C step. $\delta^{30}Si_{melt}$ is the initial $\delta^{30}Si$ of the melt. In this case $\delta^{30}Si_{melt}$ = -0.22 ‰ for SiO_2 = 58 wt%.

Our model is in good agreement with the measured silicon isotopic trend in terrestrial lavas (Fig. 13b). The linear trend of our model (y = 0.0061 x – 0.588) is close to the linear trend measured of the Hekla volcanic suite (y = 0.0059 x – 0.591; Savage et al. (2011)) and Cedar Butte volcanic suite (y = 0.0069x – 0.638; Zambardi et al. (2014)). The sharp $\delta^{30}Si$ increase observed in the model at 74wt% SiO_2 is directly correlated to the beginning of quartz crystallization associated with a decrease of anorthite and albite crystallization. Our new set of fractionation factors between silicate minerals and melts allow us to better constrain the fractional crystallization model for the first time. Besides the source effect discussed above, it shows that fractional crystallization may explain the observed heavy silicon isotope signature in the most evolved lavas (Fig. 13b), at variance with the previous interpretation of Zambardi et al. (2014) for the Cedar Butte volcanic suite.

5.2 – Partial melting effect on iron isotopes

Previous studies have suggested that mantle-derived melts may show heavier iron isotope signatures compared to their presumed mantle peridotite source rocks (e.g. Williams et al., 2004; Weyer and Ionov, 2007; Williams et al., 2009; Dauphas et al., 2014; Williams and Bizimis, 2014; Sossi et al., 2016; Nebel et al., 2018). The changes in Fe^{3+}/Fe_{tot} between crystal and liquid due to partial melting has been argued as a key parameter to explain this. The moderately incompatible behavior of Fe^{3+} (Kd = C_{melt}/C_{solid} ~4.5; Mallmann and O'Neill, 2009; Cottrell and Kelley, 2011) relative to Fe^{2+} iron (Kd = 1; Mallmann and O'Neill, 2009; Davis et al., 2013) suggests that iron isotope fractionation could occur during partial melting of upper-mantle to create oceanic crust. Many studies using different models (i.e. batch-melting, non-modal melting; e.g. Weyer and Ionov, 2007; Williams et al., 2009; Dauphas et al., 2014; Williams and Bizimis, 2014; Sossi et al., 2016), tried to assess whether partial melting of mantle peridotite, through single or numerous stages, could create the heavier isotopic signature of MORB (0.7 ‰ < $\delta^{57}Fe$ < 0.22 ‰; Sossi et al. 2016). However, the role of partial melting on the iron isotope signature of MORB remains debated (e.g. Weyer and Ionov, 2007; Williams et al., 2009; Dauphas et al., 2014; Williams and Bizimis, 2014; Sossi et al., 2016). Many parameters in these partial melting models are well constrained such as the Fe^{3+}/Fe_{tot} of MORB (Fe^{3+}/Fe_{tot} = 0.09 ± 0.02; Bézos et al., 2021) and the temperature at depth during mantle melting. One of the main critical parameters is the fractionation factor between the melt and the minerals (olivine, orthopyroxene). A recent study by Dauphas et al. (2014) shows that partial melting is only responsible for one third (0.023 ‰) of the isotopic fractionation between MORB and mantle peridotite. Sossi et al. (2016) proposed a correction of Fe isotope signature of MORB for the effect of olivine early fractionation allowing them to assess whether mantle heterogeneity could be the source of the heavy iron isotope signature of MORB. From this correction, it appears that normal MORB displays a mean $\delta^{57}Fe$ of 0.10 ± 0.01 ‰. Sossi et al. (2016) demonstrated then that for an upper mantle $\delta^{57}Fe$ = 0.05 ± 0.01 ‰, a Fe^{3+}/Fe_{tot} = 0.037 and a degree of partial melting comprised between 0.1 and 0.2, the MORB iron isotope composition can be reproduced. As mentioned above, the choice of $\Delta^{57}Fe_{min\text{-}melt}$ is critical in partial melting models. Sossi et al. (2016) applied a $\Delta^{57}Fe_{min\text{-}melt} = \Delta^{57}Fe_{ol\text{-}melt} = -0.4 \times 10^6/T^2$ as olivine is the major iron carrier in peridotites before orthopyroxene. At 1500 K, the $\Delta^{57}Fe_{ol\text{-}melt}$ is about -0.17 ‰ in their models, which is slightly higher, but similar within uncertainties, than our calculated $\Delta^{57}Fe_{forsterite\text{-}basalt\_IR} = \Delta^{57}Fe_{orthoenstatite\text{-}basalt\_IR}$ = -0.15 ‰. Our new set of equilibrium isotope fractionation factor between minerals and melts allows us to confirm that normal MORB iron isotopic signature can be explained by 10 to 20 % partial melting of the peridotite mantle as demonstrated by Sossi et al. (2016).

5.3 – Iron isotope intracrystalline diffusion

Chemical zoning is commonly observed in phenocrysts (i.e. olivine, pyroxene) of volcanic rocks. This has been interpreted as the result of crystal growth in an evolving melt during magmatic differentiation or/and diffusion-controlled chemical exchange due to the contrast (disequilibrium) between crystal and melt composition (e.g. Teng et al., 2011). In the past few years, studies demonstrated that iron chemical zoning in olivine is mirrored by iron isotope zoning (Teng et al., 2011; Sio et al., 2013; Oeser et al., 2014; Oeser et al., 2015; Collinet et al., 2017; Sio et al., 2018; Oeser et al., 2018). Iron isotopes profiles across olivine display significant variations (> 1 ‰; Oeser et al., 2015; Oeser et al., 2018) that exceeds potential equilibrium isotope fractionation. Iron isotopes profiles can therefore be used as evidence for the diffusion origin of the chemical zoning in olivine, since the light isotopes (^{54}Fe) diffuse faster than the heavy isotopes (^{57}Fe) (e.g. Richter et al. 2003). Quantifying kinetic isotope effects in minerals and melts from first-principles calculations, as performed in recent studies for other elements (e.g. Luo et al., 2021, 2020; Spallanzani et al., 2022), is beyond the scope of this study. We would require a large simulation cell for the melt with an important number of atoms (N) in order to assess with precision diffusion coefficients for the different elements in our systems, as diffusivity follows the inverse of $N^{1/3}$ dependence (Karki, 2010). However, from our set of iron equilibrium fractionation factors between silicate melts and minerals, we can assess the magnitude of iron isotope fractionation during olivine crystallization over diffusion-driven kinetic isotope fractionation. The net isotope fractionation measured across zoned olivine crystals depends on the rate of crystal growth relative to the rate of chemical diffusion (Sio et al., 2013; Sio and Dauphas, 2017). A fast crystal growth relative to diffusion process would generate olivine zoning driven by crystal growth associated with magmatic differentiation. Some authors (Dauphas et al., 2014; Prissel et al., 2018; Sio et al., 2018), implied that in this case only little isotopic fractionation between mineral and melt is expected as they consider $\Delta^{57}Fe_{olivine\text{-}melt}$ to be insignificant at magmatic temperature. Alternatively, when crystal growth is slow relative to diffusion, then crystal zoning is induced by diffusive re-equilibration with the evolving melts and higher isotopic variations within the olivine are expected. The lack of fractionation between forsterite and melt was also observed in our study in the case of a basaltic melt with low iron content, basalt_ID, with a $\Delta^{57}Fe_{forsterite\text{-}basalt\text{-}ID}$ = -0.01 ‰ at 1500 K. Our study shows however that the equilibrium fractionation factors between olivine and a basalt with higher iron content (13.1 wt%) are significant with a $\Delta^{57}Fe_{forsterite\text{-}basalt\_IR}$ = -0.15 ‰ and a $\Delta^{57}Fe_{hortonolite\text{-}basalt\_IR}$ = -0.18 ‰ at 1500 K. Therefore, at equilibrium, considering that iron isotope fractionation is exclusively driven by crystal growth process, an olivine may display according to our calculation δ^{57}Fe as low as -0.09 ‰, considering a melt value of 0.09 ‰ (BIR1g, Craddock and Dauphas, 2011; Oeser et al., 2014). Iron isotopes composition lighter than -0.09 ‰, as observed in in-situ isotopic profiles with olivine rims δ^{57}Fe as low as -2.1 ‰ (Oeser et al., 2015), can therefore only be explained by diffusion-driven fractionation (Oeser et al., 2015; Collinet et al., 2017b; Sio and Dauphas, 2017; Prissel et al., 2018).

Our new equilibrium $\Delta^{57}Fe_{olivine\text{-}basalt\_IR}$ allows us to propose that the low δ^{57}Fe signatures observed in olivines can in part be explained by equilibrium fractionation. However, our results also confirm that kinetic diffusion-driven fractionation has a major influence on the iron isotope chemical profiles of olivine as implied by other studies (Teng et al., 2011; Sio et al., 2013; Oeser et al., 2015; Collinet et al., 2017a; Sio and Dauphas, 2017; Prissel et al., 2018; Sio et al., 2018; Oeser et al., 2018). As discussed above in section 5.5.1.1 and underlined by Nebel et al. (2018), although diffusion in olivine can create large isotopic variations at the crystal scale, it is not expected to affect significantly (> 0.03 ‰) the melt composition during magmatic differentiation as proposed by Lundstrom (2009) and Zambardi et al. (2014).

6- Conclusion

This study provides, for the first time, equilibrium Fe and Si isotope β-factors of various melts, using first-principles molecular dynamics. We first demonstrated, through comparison of the “snapshot” and “VAF” methods, that both methods are appropriate to study isotope fractionation of melts. Iron, that acts mainly as a network-modifier in the melts, displays significant isotope fractionation among the

different compositions of melt. The Fe-O mean coordination number appears not playing a significant role on the observed Fe β-factor variations in melts. The main parameters driving the iron isotope composition in melts is the Fe-O bond length. The chemical environment around iron (i.e. iron second neighbors) is also suggested to contribute to Fe isotope fractionation, as smaller Fe-Fe and Fe-Mg distances leads to higher Fe β-factor values in the melts. Further investigations are necessary in order to confirm this hypothesis. Overall, these results show that significant Fe isotope fractionation is expected without changes of iron redox. On the other hand, silicon isotope fractionation appears to be less sensitive to compositional changes in melts and displays limited isotope fractionation among the different melts. This is most likely due to its network-former role in the melt. Since structural parameters such as Si-O bond length and coordination number remain constant, they do not play a major role on the Si β-factors variation observed in these melts. The silicon isotope compositional variations were also expected to be related to the depolymerization degree (NBO/T; Grant, 1954; Poitrasson and Zambardi, 2015). However, this relationship may be blurred by the high alkaline content of the melts. Silicon β-factors appear to be also driven by its local environment, notably the presence of iron as silicon second neighbors.

This Fe and Si β-factors of melts allowed us to calculate a consistent set of equilibrium fractionation factors between various minerals and melts. This represents a major step forward in the understanding and quantifying of the processes involved in iron and silicon isotope fractionation in magmatic settings. In this perspective, we used our new $\Delta^{57}Fe_{min\text{-}melt}$ and $\Delta^{30}Si_{min\text{-}melt}$ in several models from the literature in order to assess the impact of the addition of more constrained fractionation factors on them. Our results support fractional crystallization as a possible driving process involved in both Si and Fe isotope evolution during magmatic differentiation for the melts chemical range investigated. Our calculated $\Delta^{57}Fe_{ol\text{-}melt}$ allows us to confirm the model of Sossi et al. (2016) showing that generation of MORB with $\delta^{57}Fe$ = 0.1 ‰ can be explained by partial melting of peridotites (with a degree of partial melting comprised between 10 and 20%). This different from nil $\Delta^{57}Fe_{ol\text{-}melt}$ fractionation factor however contradicts Prissel et al. (2018) conclusions, thus calling for further investigations. We also showed that there is significant iron isotope fractionation between Fe^{2+}-bearing minerals and melts. Olivine crystallization at equilibrium could show a $\Delta^{57}Fe_{olivine\text{-}basalt}$ range from 0 to -0.18 ‰. Our new set of iron fractionation factors can therefore help to quantify the equilibrium fractionation versus the diffusion-driven kinetic fractionation in future iron isotope diffusion models.

APPENDIX A. SUPPLEMENTARY MATERIAL

The file includes all the parameters and discussions relative to the structural properties of the melts (including MSDs and RDFs).

APPENDIX B. SUPPLEMENTARY MATERIAL

The file includes the Fe and Si fractionation factors between the different melts and silicate minerals as well as the detailed calculation of the fractionation factors (systematic bias correction).

APPENDIX C. SUPPLEMENTARY MATERIAL

This MS Excel file includes Fe and Si fractional crystallization results and VAF iron beta fractionation factors.

ACKNOWLEDGEMENT

We thank the associate editor Dr. Fang Huang and the three anonymous reviewers for their detailed and thoughtful reviews that improved this manuscript. This work was supported by the ECOS-NORD/COLCIENCIAS French-Colombian cooperation program (Project number: C17U01). CP also acknowledges funding from COLCIENCIAS through research grants No. 2015-710-51568. This work was also supported through a grant to FP from the "Programme National de Planétologie-PNP" of CNRS/INSU, co-funded by CNES. Calculations were performed using the HPC resources from CALMIP (Grant 2020 – P1037). SR deeply thanks CALMIP staff for their support.

REFERENCES

Allen M. P. and Tildesley D. J. (1989) Computer simulation of liquids. *J. Solution Chem.* **18**, 99. Available at: https://doi.org/10.1007/BF00646086.

Angeli F., Villain O., Schuller S., Ispas S. and Charpentier T. (2011) Insight into sodium silicate glass structural organization by multinuclear NMR combined with first-principles calculations. *Geochim. Cosmochim. Acta* **75**, 2453–2469.

Bajgain S., Ghosh D. B. and Karki B. B. (2015) Structure and density of basaltic melts at mantle conditions from first-principles simulations. *Nat. Commun.* **6**, 1–7. Available at: http://dx.doi.org/10.1038/ncomms9578.

Bauchy M. and Micoulaut M. (2011) Atomic scale foundation of temperature-dependent bonding constraints in network glasses and liquids. *J. Non. Cryst. Solids* **357**, 2530–2537. Available at: http://dx.doi.org/10.1016/j.jnoncrysol.2011.03.017.

Bertka C. M. and Holloway J. R. (1994) Anhydrous partial melting of an iron-rich mantle I: subsolidus phase assemblages and partial melting phase relations at 10 to 30 kbar. *Contrib. to Mineral. Petrol.* **115**, 313–322. Available at: https://doi.org/10.1007/BF00310770.

Bézos A., Guivel C., La C., Fougeroux T. and Humler E. (2021) Unraveling the confusion over the iron oxidation state in MORB glasses. *Geochim. Cosmochim. Acta* **293**, 28–39.

Bézos A. and Humler E. (2005) The Fe3+/ΣFe ratios of MORB glasses and their implications for mantle melting. *Geochim. Cosmochim. Acta* **69**, 711–725.

Bigeleisen J. and Mayer M. G. (1947) Calculation of Equilibrium Constants for Isotopic Exchange Reactions. *J. Chem. Phys.* **15**, 261–267. Available at: https://doi.org/10.1063/1.1746492.

Blanchard M., Balan E. and Schauble E. A. (2017) Equilibrium Fractionation of Non-traditional Isotopes: a Molecular Modeling Perspective. *Rev. Mineral. Geochemistry* **82**, 27–63. Available at: https://doi.org/10.2138/rmg.2017.82.2.

Bohrson W. A., Spera F. J., Ghiorso M. S., Brown G. A., Creamer J. B. and Mayfield A. (2014) Thermodynamic model for energy-constrained open-system evolution of crustal magma bodies undergoing simultaneous recharge, assimilation and crystallization: The magma chamber simulator. Journal of Petrology 55, 1685–1717.

Caracas R., Hirose K., Nomura R. and Ballmer M. D. (2019) Melt–crystal density crossover in a deep magma ocean. *Earth Planet. Sci. Lett.* **516**, 202–211. Available at: https://doi.org/10.1016/j.epsl.2019.03.031.

Collinet M., Charlier B., Namur O., Oeser M., Médard E. and Weyer S. (2017a) Crystallization history of enriched shergottites from Fe and Mg isotope fractionation in olivine megacrysts. *Geochim. Cosmochim. Acta* **207**, 277–297. Available at: http://dx.doi.org/10.1016/j.gca.2017.03.029.

Collinet M., Charlier B., Namur O., Oeser M., Médard E. and Weyer S. (2017b) Crystallization history of enriched shergottites from Fe and Mg isotope fractionation in olivine megacrysts. *Geochim. Cosmochim. Acta* **207**, 277–297.

Cottrell E. and Kelley K. A. (2014) Redox Heterogeneity of the Mantle Inferred from Hotspots. In *AGU Fall Meeting Abstracts* pp. V23G-02.

Cottrell E. and Kelley K. A. (2011) The oxidation state of Fe in MORB glasses and the oxygen fugacity of the upper mantle. *Earth Planet. Sci. Lett.* **305**, 270–282. Available at: http://dx.doi.org/10.1016/j.epsl.2011.03.014.

Craddock P. R. and Dauphas N. (2011) Iron and carbon isotope evidence for microbial iron respiration throughout the Archean. *Earth Planet. Sci. Lett.* **303**, 121–132. Available at: http://www.sciencedirect.com/science/article/pii/S0012821X10008186.

Dauphas N., Roskosz M., Alp E. E., Golden D. C., Sio C. K., Tissot F. L. H., Hu M. Y., Zhao J., Gao L. and Morris R. V. (2012) A general moment NRIXS approach to the determination of equilibrium Fe isotopic fractionation factors: Application to goethite and jarosite. *Geochim. Cosmochim. Acta* **94**, 254–275.

Dauphas N., Roskosz M., Alp E. E., Neuville D. R., Hu M. Y., Sio C. K., Tissot F. L. H., Zhao J., Tissandier

L., Médard E. and Cordier C. (2014) Magma redox and structural controls on iron isotope variations in Earth's mantle and crust. *Earth Planet. Sci. Lett.* **398**, 127–140.

Davis F. A., Humayun M., Hirschmann M. M. and Cooper R. S. (2013) Experimentally determined mineral/melt partitioning of first-row transition elements (FRTE) during partial melting of peridotite at 3GPa. *Geochim. Cosmochim. Acta* **104**, 232–260. Available at: http://dx.doi.org/10.1016/j.gca.2012.11.009.

Deng Z., Chaussidon M., Guitreau M., Puchtel I. S., Dauphas N. and Moynier F. (2019) An oceanic subduction origin for Archaean granitoids revealed by silicon isotopes. *Nat. Geosci.* **12**, 774–778. Available at: http://dx.doi.org/10.1038/s41561-019-0407-6.

Du D. H., Wang X. L., Yang T., Chen X., Li J. Y. and Li W. (2017) Origin of heavy Fe isotope compositions in high-silica igneous rocks: A rhyolite perspective. *Geochim. Cosmochim. Acta* **218**, 58–72. Available at: https://doi.org/10.1016/j.gca.2017.09.014.

Ducher M., Blanchard M. and Balan E. (2018) Equilibrium isotopic fractionation between aqueous Zn and minerals from first-principles calculations. *Chem. Geol.* **483**, 342–350. Available at: https://doi.org/10.1016/j.chemgeo.2018.02.040.

Dupuis R., Benoit M., Nardin E. and Méheut M. (2015) Fractionation of silicon isotopes in liquids: The importance of configurational disorder. *Chem. Geol.* **396**, 239–254. Available at: http://www.sciencedirect.com/science/article/pii/S0009254115000029.

Feng S., Majumdar A., Kuang H., Pan Y., Iitaka T. and Tse J. S. (2021) A comparative study on pressure-induced structural transformations in a basaltic glass and melt from Ab initio molecular dynamics calculations. *Phys. Chem. Miner.* **48**, 1–14. Available at: https://doi.org/10.1007/s00269-021-01165-3.

Foden J., Sossi P. A. and Wawryk C. M. (2015) Fe isotopes and the contrasting petrogenesis of A-, I- and S-type granite. *Lithos* **212**–**215**, 32–44. Available at: http://dx.doi.org/10.1016/j.lithos.2014.10.015.

Gajos N. A., Lundstrom C. C. and Taylor A. H. (2016) Spatially controlled Fe and Si isotope variations: an alternative view on the formation of the Torres del Paine pluton. *Contrib. to Mineral. Petrol.* **171**.

Gerlach S., Claußen O. and Russel C. (1998) Self-diffusion of iron in alkali – magnesia – silica glass melts. *J. Non. Cryst. Solids* **226**, 11–18.

Ghosh D. B. and Karki B. B. (2020) Effects of valence and spin of Fe in MgSiO3 melts: Structural insights from first-principles molecular dynamics simulations. *Geochim. Cosmochim. Acta* **279**, 107–118. Available at: https://doi.org/10.1016/j.gca.2020.03.040.

Ghosh D. B. and Karki B. B. (2018) First-principles molecular dynamics simulations of anorthite (CaAl2Si2O8) glass at high pressure. *Phys. Chem. Miner.* **45**, 575–587. Available at: http://dx.doi.org/10.1007/s00269-018-0943-4.

Grant F. S. (1954) The geological significance of variations in the abundances of the isotopes of silicon in rocks. *Geochim. Cosmochim. Acta* **5**, 225–242. Available at: http://www.sciencedirect.com/science/article/pii/0016703754900460.

Guillot B. and Sator N. (2007a) A computer simulation study of natural silicate melts. Part I: Low pressure properties. *Geochim. Cosmochim. Acta* **71**, 1249–1265.

Guillot B. and Sator N. (2007b) A computer simulation study of natural silicate melts. Part II: High pressure properties. *Geochim. Cosmochim. Acta* **71**, 4538–4556.

He Y., Wu H., Ke S., Liu S. A. and Wang Q. (2017) Iron isotopic compositions of adakitic and non-adakitic granitic magmas: Magma compositional control and subtle residual garnet effect. *Geochim. Cosmochim. Acta* **203**, 89–102. Available at: http://dx.doi.org/10.1016/j.gca.2017.01.005.

Heimann A., Beard B. L. and Johnson C. M. (2008) The role of volatile exsolution and sub-solidus fluid/rock interactions in producing high 56Fe/54Fe ratios in siliceous igneous rocks. *Geochim. Cosmochim. Acta* **72**, 4379–4396.

Huang F., Wu Z., Huang S. and Wu F. (2014) First-principles calculations of equilibrium silicon isotope fractionation among mantle minerals. *Geochim. Cosmochim. Acta* **140**, 509–520. Available at: http://dx.doi.org/10.1016/j.gca.2014.05.035.

Jackson W. E., Farges F., Yeager M., Mabrouk P. A., Rossano S., Waychunas G. A., Solomon E. I. and Brown G. E. (2005) Multi-spectroscopic study of Fe(II) in silicate glasses: Implications for the coordination environment of Fe(II) in silicate melts. *Geochim. Cosmochim. Acta* **69**, 4315–4332.

Karki B. B. (2015) First-principles computation of mantle materials in crystalline and amorphous phases. *Phys. Earth Planet. Inter.* **240**, 43–69.

Karki B. B. (2010) First-principles molecular dynamics simulations of silicate melts: Structural and dynamical properties. *Theor. Comput. Methods Miner. Phys. Geophys. Appl.* **71**, 355–389.

Karki B. B., Ghosh D. B., Maharjan C., Karato S. I. and Park J. (2018) Density-Pressure Profiles of Fe-Bearing MgSiO3 Liquid: Effects of Valence and Spin States, and Implications for the Chemical Evolution of the Lower Mantle. *Geophys. Res. Lett.* **45**, 3959–3966.

Kelley D. F. and Barton M. (2008) Pressures of crystallization of Icelandic Magmas. *J. Petrol.* **49**, 465–492.

Kim H. I., Sur J. C. and Lee S. K. (2016) Effect of iron content on the structure and disorder of iron-bearing sodium silicate glasses: A high-resolution 29Si and 17O solid-state NMR study. *Geochim. Cosmochim. Acta* **173**, 160–180. Available at: http://dx.doi.org/10.1016/j.gca.2015.10.023.

Konter J. G., Pietruszka A. J., Hanan B. B., Finlayson V. A., Craddock P. R., Jackson M. G. and Dauphas N. (2016) Unusual δ56Fe values in Samoan rejuvenated lavas generated in the mantle. *Earth Planet. Sci. Lett.* **450**, 221–232. Available at: http://dx.doi.org/10.1016/j.epsl.2016.06.029.

Kowalski P. M. and Jahn S. (2011) Prediction of equilibrium Li isotope fractionation between minerals and aqueous solutions at high P and T: An efficient ab initio approach. *Geochim. Cosmochim. Acta* **75**, 6112–6123. Available at: http://dx.doi.org/10.1016/j.gca.2011.07.039.

Kresse G. and Furthmüller J. (1996) Efficient iterative schemes for ab initio total-energy calculations using a plane-wave basis set. *Phys. Rev. B* **54**, 11169–11186. Available at: https://link.aps.org/doi/10.1103/PhysRevB.54.11169.

Kresse G. and Joubert D. (1999) From ultrasoft pseudopotentials to the projector augmented-wave method. *Phys. Rev. B* **59**, 1758–1775. Available at: https://link.aps.org/doi/10.1103/PhysRevB.59.1758.

Kuryaeva R. G. (2004) Degree of polymerization of aluminosilicate glasses and melts. *Glas. Phys. Chem.* **30**, 157–166.

Landau L. D. and Lifshitz E. M. (1980) Course of Theoretical Physics. Statistical Physics. Part 1. Pergamon 5. , 544.

Li Q. W., Zhao J. H., Wang Q., Zhang Z. F., An Y. J. and He Y. T. (2020) Iron isotope fractionation in hydrous basaltic magmas in deep crustal hot zones. *Geochim. Cosmochim. Acta* **279**, 29–44. Available at: https://doi.org/10.1016/j.gca.2020.03.032.

Le Losq C., Neuville D. R., Florian P., Henderson G. S. and Massiot D. (2014) The role of Al3+ on rheology and structural changes in sodium silicate and aluminosilicate glasses and melts. *Geochim. Cosmochim. Acta* **126**, 495–517. Available at: http://dx.doi.org/10.1016/j.gca.2013.11.010.

Lundstrom C. (2009) Hypothesis for the origin of convergent margin granitoids and Earth's continental crust by thermal migration zone refining. *Geochim. Cosmochim. Acta* **73**, 5709–5729. Available at: https://www.sciencedirect.com/science/article/pii/S0016703709004116 [Accessed April 26, 2019].

Luo, H., Karki, B. B., Ghosh, D. B., and Bao, H.: First-principles computation of diffusional Mg isotope fractionation in silicate melts, Geochimica et Cosmochimica Acta, 290, 27–40, https://doi.org/10.1016/j.gca.2020.08.028, 2020.

Luo, H., Karki, B. B., Ghosh, D. B., and Bao, H.: Deep neural network potentials for diffusional lithium isotope fractionation in silicate melts, Geochimica et Cosmochimica Acta, 303, 38–50, https://doi.org/10.1016/j.gca.2021.03.031, 2021.

Macris C. A., Manning C. E. and Young E. D. (2015) Crystal chemical constraints on inter-mineral Fe isotope fractionation and implications for Fe isotope disequilibrium in San Carlos mantle xenoliths. *Geochim. Cosmochim. Acta* **154**, 168–185. Available at: http://dx.doi.org/10.1016/j.gca.2015.01.024.

Mallmann G. and O'Neill H. S. C. (2009) The crystal/melt partitioning of V during mantle melting as a

function of oxygen fugacity compared with some other elements (Al, P, Ca, Sc, Ti, Cr, Fe, Ga, Y, Zr and Nb). *J. Petrol.* **50**, 1765–1794.
Matsui M. (1994) A Transferable Interatomic Potential Model for Crystals and Melts in the System CaO-MgO-Al2O3-SiO2. *Mineral. Mag.* **58A**, 571–572.
McMillan P. (1984) Structural studies of silicate glasses and melts-applications and limitations of Raman spectroscopy. *Am. Mineral.* **69**, 622–644.
Méheut M., Lazzeri M., Balan E. and Mauri F. (2009) Structural control over equilibrium silicon and oxygen isotopic fractionation: A first-principles density-functional theory study. *Chem. Geol.* **258**, 28–37. Available at: http://dx.doi.org/10.1016/j.chemgeo.2008.06.051.
Méheut M. and Schauble E. A. (2014) Silicon isotope fractionation in silicate minerals: Insights from first-principles models of phyllosilicates, albite and pyrope. *Geochim. Cosmochim. Acta* **134**, 137–154. Available at: http://dx.doi.org/10.1016/j.gca.2014.02.014.
Meyer R. and Comtesse D. (2011) Vibrational density of states of silicon nanoparticles. *Phys. Rev. B - Condens. Matter Mater. Phys.* **83**, 1–6.
Mysen B. O. (2006) The structural behavior of ferric and ferrous iron in aluminosilicate glass near meta-aluminosilicate joins. *Geochim. Cosmochim. Acta* **70**, 2337–2353.
Mysen B. O., Lucier A. and Cody G. D. (2003) The structural behavior of Al3+ in peralkaline melts and glasses in the system Na2O-Al2O3-SiO2. *Am. Mineral.* **88**, 1668–1678. Available at: https://doi.org/10.2138/am-2003-11-1206.
Mysen B. and Richet P. (2019a) *Properties of Aluminosilicate Systems.*, *Silic. Glas. Melts,263-300.*
Mysen B. and Richet P. (2019b) Structure of Iron Silicate Glasses and Melts. *Silic. Glas. Melts*, 403–430.
Nebel O., Sossi P. A., Bénard A., Wille M., Vroon P. Z. and Arculus R. J. (2015) Redox-variability and controls in subduction zones from an iron-isotope perspective. *Earth Planet. Sci. Lett.* **432**, 142–151. Available at: http://dx.doi.org/10.1016/j.epsl.2015.09.036.
Nebel O., Sossi P. A., Foden J., Bénard A., Brandl P. A., Stammeier J. A., Lupton J., Richter M. and Arculus R. J. (2018) Iron isotope variability in ocean floor lavas and mantle sources in the Lau back-arc basin. *Geochim. Cosmochim. Acta* **241**, 150–163.
Nosé S. (1984) A unified formulation of the constant temperature molecular dynamics methods. *J. Chem. Phys.* **81**, 511–519. Available at: https://doi.org/10.1063/1.447334.
Oeser M., Dohmen R., Horn I., Schuth S. and Weyer S. (2015) Processes and time scales of magmatic evolution as revealed by Fe-Mg chemical and isotopic zoning in natural olivines. *Geochim. Cosmochim. Acta* **154**, 130–150. Available at: http://dx.doi.org/10.1016/j.gca.2015.01.025.
Oeser M., Ruprecht P. and Weyer S. (2018) Combined Fe-Mg chemical and isotopic zoning in olivine constraining magma mixing-to-eruption timescales for the continental arc volcano Irazú (Costa Rica) and Cr diffusion in olivine. *Am. Mineral.* **103**, 582–599.
Oeser M., Weyer S., Horn I. and Schuth S. (2014) High-precision fe and mg isotope ratios of silicate reference glasses determined in situ by femtosecond LA-MC-ICP-MS and by solution nebulisation MC-ICP-MS. *Geostand. Geoanalytical Res.* **38**, 311–328.
Oestrike R., Yang W. hong, Kirkpatrick R. J., Hervig R. L., Navrotsky A. and Montez B. (1987) High-resolution 23Na, 27Al and 29Si NMR spectroscopy of framework Aluminosilicate glasses. *Geochim. Cosmochim. Acta* **51**, 2199–2209.
Perdew J. P., Burke K. and Ernzerhof M. (1996) Generalized gradient approximation made simple. *Phys. Rev. Lett.* **77**, 3865–3868.
Pichavant M. (2002) Physical conditions, structure, and dynamics of a zoned magma chamber: Mount Pelée (Martinique, Lesser Antilles Arc). *J. Geophys. Res.* **107**.
Pinilla C., Blanchard M., Balan E., Natarajan S. K., Vuilleumier R. and Mauri F. (2015) Equilibrium magnesium isotope fractionation between aqueous Mg2+ and carbonate minerals: Insights from path integral molecular dynamics. *Geochim. Cosmochim. Acta* **163**, 126–139.
Pinilla C., De Moya A., Rabin S., Morard G., Roskosz M. and Blanchard M. (2021) First-principles investigation of equilibrium iron isotope fractionation in Fe(1-x)Sx alloys at Earth's core formation conditions. *Earth Planet. Sci. Lett.* **569**, 117059.
Poitrasson F. (2017) Silicon Isotope Geochemistry. *Rev. Mineral. Geochemistry* **82**, 289–344. Available

at: https://doi.org/10.2138/rmg.2017.82.8.
Poitrasson F. and Freydier R. (2005) Heavy iron isotope composition of granites determined by high resolution MC-ICP-MS. *Chem. Geol.* **222**, 132–147. Available at: https://linkinghub.elsevier.com/retrieve/pii/S0009254105002615.
Poitrasson F. and Zambardi T. (2015) An Earth-Moon silicon isotope model to track silicic magma origins. *Geochim. Cosmochim. Acta* **167**, 301–312. Available at: http://dx.doi.org/10.1016/j.gca.2015.07.005.
Polyakov V. B. and Mineev S. D. (2000) The use of Mossbauer spectroscopy in stable isotope geochemistry. *Geochim. Cosmochim. Acta* **64**, 849–865.
Prissel K. B., Krawczynski M. J., Nie N. X., Dauphas N., Couvy H., Hu M. Y., Alp E. E. and Roskosz M. (2018) Experimentally determined effects of olivine crystallization and melt titanium content on iron isotopic fractionation in planetary basalts. *Geochim. Cosmochim. Acta* **238**, 580–598.
Qin T., Wu F., Wu Z. and Huang F. (2016) First-principles calculations of equilibrium fractionation of O and Si isotopes in quartz, albite, anorthite, and zircon. *Contrib. to Mineral. Petrol.* **171**.
Rabin S., Blanchard M., Pinilla C., Poitrasson F. and Grégoire M. (2021) First-principles calculation of iron and silicon isotope fractionation between Fe-bearing minerals at magmatic temperatures: The importance of second atomic neighbors. *Geochim. Cosmochim. Acta* **304**, 101–118.
Richter F. M., Davis A. M., DePaolo D. J. and Watson E. B. (2003) Isotope fractionation by chemical diffusion between molten basalt and rhyolite. *Geochimica et Cosmochimica Acta* **67**, 3905–3923.
Redlich O. (1935) Eine allgemeine beziehung zwischen den schwingungsfrequenzen isotoper molekeln. *Z Phys Chem* **28**, 371–382.
Roskosz M., Dauphas N., Hu J., Hu M. Y., Neuville D. R., Brown D., Bi W., Nie N. X., Zhao J. and Alp E. E. (2022) Structural, redox and isotopic behaviors of iron in geological silicate glasses: A NRIXS study of Lamb-Mössbauer factors and force constants. *Geochim. Cosmochim. Acta* **321**, 184–205. Available at: https://doi.org/10.1016/j.gca.2022.01.021.
Roskosz M., Sio C. K. I., Dauphas N., Bi W., Tissot F. L. H., Hu M. Y., Zhao J. and Alp E. E. (2015) Spinel-olivine-pyroxene equilibrium iron isotopic fractionation and applications to natural peridotites. *Geochim. Cosmochim. Acta* **169**, 184–199.
Rossano S., Ramos A. Y. and Delaye J. M. (2000) Environment of ferrous iron in CaFeSi2O6 glass; contributions of EXAFS and molecular dynamics. *J. Non. Cryst. Solids* **273**, 48–52.
Savage P. S., Georg R. B., Williams H. M., Burton K. W. and Halliday A. N. (2011) Silicon isotope fractionation during magmatic differentiation. *Geochim. Cosmochim. Acta* **75**, 6124–6139. Available at: http://dx.doi.org/10.1016/j.gca.2011.07.043.
Savage P. S., Georg R. B., Williams H. M., Turner S., Halliday A. N. and Chappell B. W. (2012) The silicon isotope composition of granites. *Geochim. Cosmochim. Acta* **92**, 184–202. Available at: http://dx.doi.org/10.1016/j.gca.2012.06.017.
Schoenberg R., Marks M. A. W., Schuessler J. A., von Blanckenburg F. and Markl G. (2009) Fe isotope systematics of coexisting amphibole and pyroxene in the alkaline igneous rock suite of the Ilímaussaq Complex, South Greenland. *Chem. Geol.* **258**, 65–77. Available at: https://www.sciencedirect.com/science/article/pii/S0009254108002416 [Accessed April 26, 2019].
Schuessler J. A., Schoenberg R. and Sigmarsson O. (2009) Iron and lithium isotope systematics of the Hekla volcano, Iceland - Evidence for Fe isotope fractionation during magma differentiation. *Chem. Geol.* **258**, 78–91. Available at: http://dx.doi.org/10.1016/j.chemgeo.2008.06.021.
Shahar A., Young E. D. and Manning C. E. (2008) Equilibrium high-temperature Fe isotope fractionation between fayalite and magnetite: An experimental calibration. *Earth Planet. Sci. Lett.* **268**, 330–338. Available at: https://www.sciencedirect.com/science/article/pii/S0012821X08000435 [Accessed April 26, 2019].
Sio C. K. I. and Dauphas N. (2017) Thermal and crystallization histories of magmatic bodies by Monte Carlo inversion of Mg-Fe isotopic profiles in olivine. *Geology* **45**, 67–70.
Sio C. K. I., Dauphas N., Teng F. Z., Chaussidon M., Helz R. T. and Roskosz M. (2013) Discerning crystal growth from diffusion profiles in zoned olivine by in situ Mg-Fe isotopic analyses. *Geochim.*

Cosmochim. Acta **123**, 302–321. Available at: http://dx.doi.org/10.1016/j.gca.2013.06.008.
Sio C. K., Roskosz M., Dauphas N., Bennett N. R., Mock T. and Shahar A. (2018) The isotope effect for Mg-Fe interdiffusion in olivine and its dependence on crystal orientation, composition and temperature. *Geochim. Cosmochim. Acta* **239**, 463–480. Available at: https://doi.org/10.1016/j.gca.2018.06.024.
Smith W., Yong C. W. and Rodger P. M. (2002) DL_POLY: Application to molecular simulation. *Mol. Simul.* **28**, 385–471. Available at: https://doi.org/10.1080/08927020290018769.
Solomatova N. V. and Caracas R. (2021) Buoyancy and Structure of Volatile-Rich Silicate Melts. *J. Geophys. Res. Solid Earth* **126**, 1–14.
Solomatova N. V. and Caracas R. (2019) Pressure-Induced Coordination Changes in a Pyrolitic Silicate Melt From Ab Initio Molecular Dynamics Simulations. *J. Geophys. Res. Solid Earth* **124**, 11232–11250.
Sossi P. A., Foden J. D. and Halverson G. P. (2012) Redox-controlled iron isotope fractionation during magmatic differentiation: An example from the Red Hill intrusion, S. Tasmania. *Contrib. to Mineral. Petrol.* **164**, 757–772.
Sossi P. A., Nebel O. and Foden J. (2016) Iron isotope systematics in planetary reservoirs. *Earth Planet. Sci. Lett.* **452**, 295–308. Available at: http://dx.doi.org/10.1016/j.epsl.2016.07.032.
Sossi P. A. and O'Neill H. S. C. (2017) The effect of bonding environment on iron isotope fractionation between minerals at high temperature. *Geochim. Cosmochim. Acta* **196**, 121–143. Available at: https://www.sciencedirect.com/science/article/pii/S0016703716305324.
Spallanzani, R., Koga, K. T., Cichy, S. B., Wiedenbeck, M., Schmidt, B. C., Oelze, M., and Wilke, M.: Lithium and boron diffusivity and isotopic fractionation in hydrated rhyolitic melts, Contributions to Mineralogy and Petrology, 177, 74, https://doi.org/10.1007/s00410-022-01937-2, 2022.
Stein D. J. and Spera F. J. (1996) Molecular dynamics simulations of liquids and glasses in the system NaAlSiO4-SiO2: Physical properties and transport mechanisms. *Am. Mineral.* **81**, 284–302.
Telus M., Dauphas N., Moynier F., Tissot F. L. H., Teng F. Z., Nabelek P. I., Craddock P. R. and Groat L. A. (2012) Iron, zinc, magnesium and uranium isotopic fractionation during continental crust differentiation: The tale from migmatites, granitoids, and pegmatites. *Geochim. Cosmochim. Acta* **97**, 247–265.
Teng F.-Z., Dauphas N. and Helz R. T. (2008) Iron Isotope Fractionation During Magmatic Differentiation in Kilauea Iki Lava Lake. *Science (80-.).* **320**, 1620–1622. Available at: http://science.sciencemag.org/content/320/5883/1620.abstract.
Teng F. Z., Dauphas N., Helz R. T., Gao S. and Huang S. (2011) Diffusion-driven magnesium and iron isotope fractionation in Hawaiian olivine. *Earth Planet. Sci. Lett.* **308**, 317–324. Available at: http://dx.doi.org/10.1016/j.epsl.2011.06.003.
Togo A. and Tanaka I. (2015) First principles phonon calculations in materials science. *Scr. Mater.* **108**, 1–5. Available at: http://dx.doi.org/10.1016/j.scriptamat.2015.07.021.
Weyer S., Anbar A. D., Brey G. P., Münker C., Mezger K. and Woodland A. B. (2005) Iron isotope fractionation during planetary differentiation. *Earth Planet. Sci. Lett.* **240**, 251–264.
Weyer S. and Ionov D. A. (2007) Partial melting and melt percolation in the mantle: The message from Fe isotopes. *Earth Planet. Sci. Lett.* **259**, 119–133.
Weyer S. and Seitz H. M. (2012) Coupled lithium- and iron isotope fractionation during magmatic differentiation. *Chem. Geol.* **294–295**, 42–50. Available at: http://dx.doi.org/10.1016/j.chemgeo.2011.11.020.
Williams H. M. and Bizimis M. (2014) Iron isotope tracing of mantle heterogeneity within the source regions of oceanic basalts. *Earth Planet. Sci. Lett.* **404**, 396–407. Available at: http://dx.doi.org/10.1016/j.epsl.2014.07.033.
Williams H. M., McCammon C. A., Peslier A. H., Halliday A. N., Teutsch N., Levasseur S. and Burg J.-P. (2004) Iron Isotope Fractionation and the Oxygen Fugacity of the Mantle. *Science (80-.).* **304**, 1656 LP – 1659. Available at: http://science.sciencemag.org/content/304/5677/1656.abstract.
Williams H. M., Nielsen S. G., Renac C., Griffin W. L., O'Reilly S. Y., McCammon C. A., Pearson N., Viljoen F., Alt J. C. and Halliday A. N. (2009) Fractionation of oxygen and iron isotopes by partial melting

processes: Implications for the interpretation of stable isotope signatures in mafic rocks. *Earth Planet. Sci. Lett.* **283**, 156–166. Available at: https://www.sciencedirect.com/science/article/pii/S0012821X0900226X.

Williams H. M., Peslier A. H., McCammon C., Halliday A. N., Levasseur S., Teutsch N. and Burg J. P. (2005) Systematic iron isotope variations in mantle rocks and minerals: The effects of partial melting and oxygen fugacity. *Earth Planet. Sci. Lett.* **235**, 435–452.

Williams H. M., Prytulak J., Woodhead J. D., Kelley K. A., Brounce M. and Plank T. (2018) Interplay of crystal fractionation, sulfide saturation and oxygen fugacity on the iron isotope composition of arc lavas: An example from the Marianas. *Geochim. Cosmochim. Acta* **226**, 224–243.

Xia Y., Li S. and Huang F. (2017) Iron and Zinc isotope fractionation during magmatism in the continental crust: Evidence from bimodal volcanic rocks from Hailar basin, NE China. *Geochim. Cosmochim. Acta* **213**, 35–46. Available at: http://dx.doi.org/10.1016/j.gca.2017.06.018.

Zambardi T., Lundstrom C. C., Li X. and McCurry M. (2014) Fe and Si isotope variations at Cedar Butte volcano; insight into magmatic differentiation. *Earth Planet. Sci. Lett.* **405**, 169–179. Available at: http://dx.doi.org/10.1016/j.epsl.2014.08.020.

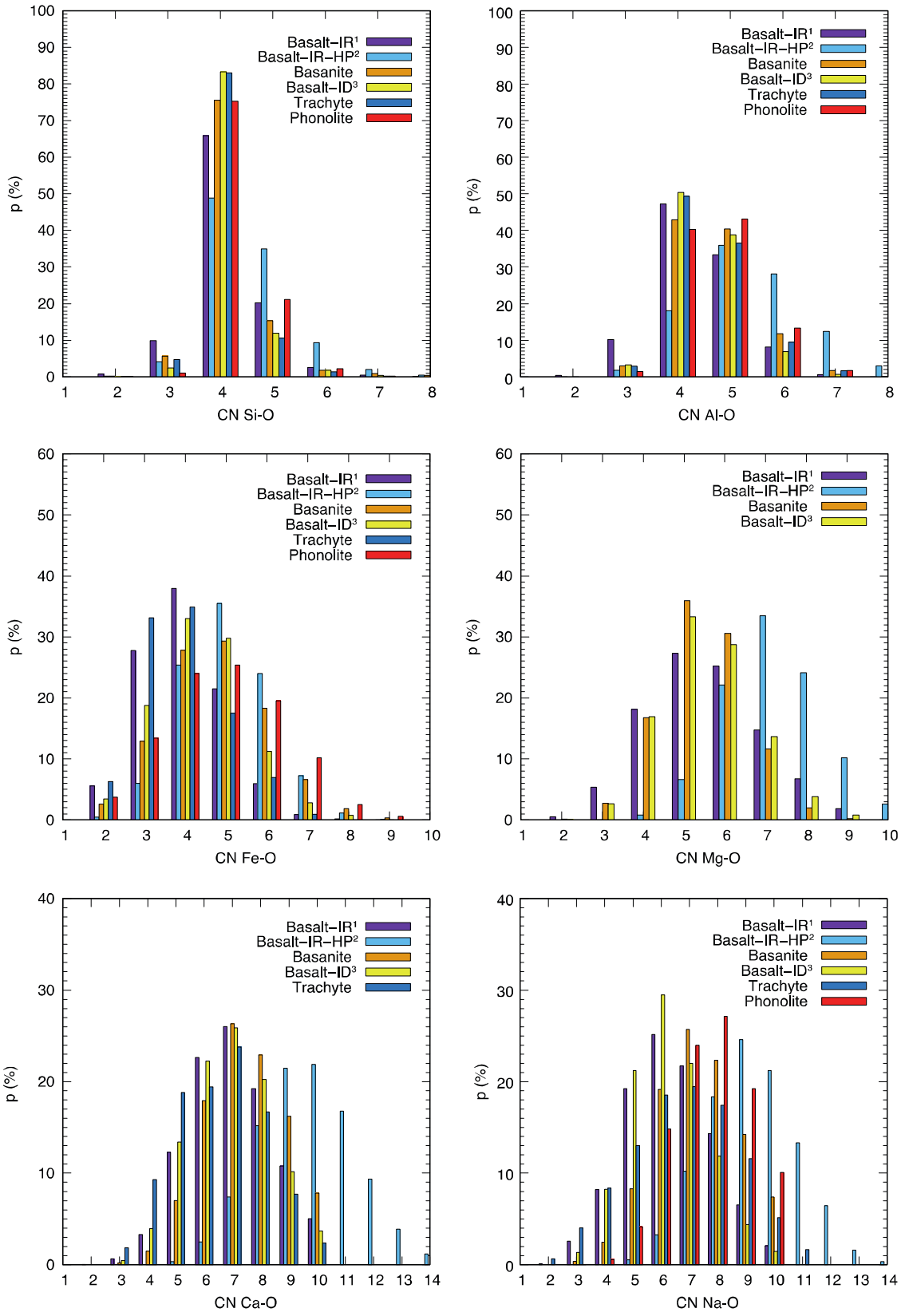

[1]Iron-rich basalt
[2]Iron-rich basalt at high-pressure (12 GPa)
[3]Iron-depleted basalt

Figure 1 - Population analysis of the cation-oxygen coordination numbers for the different simulated melts.

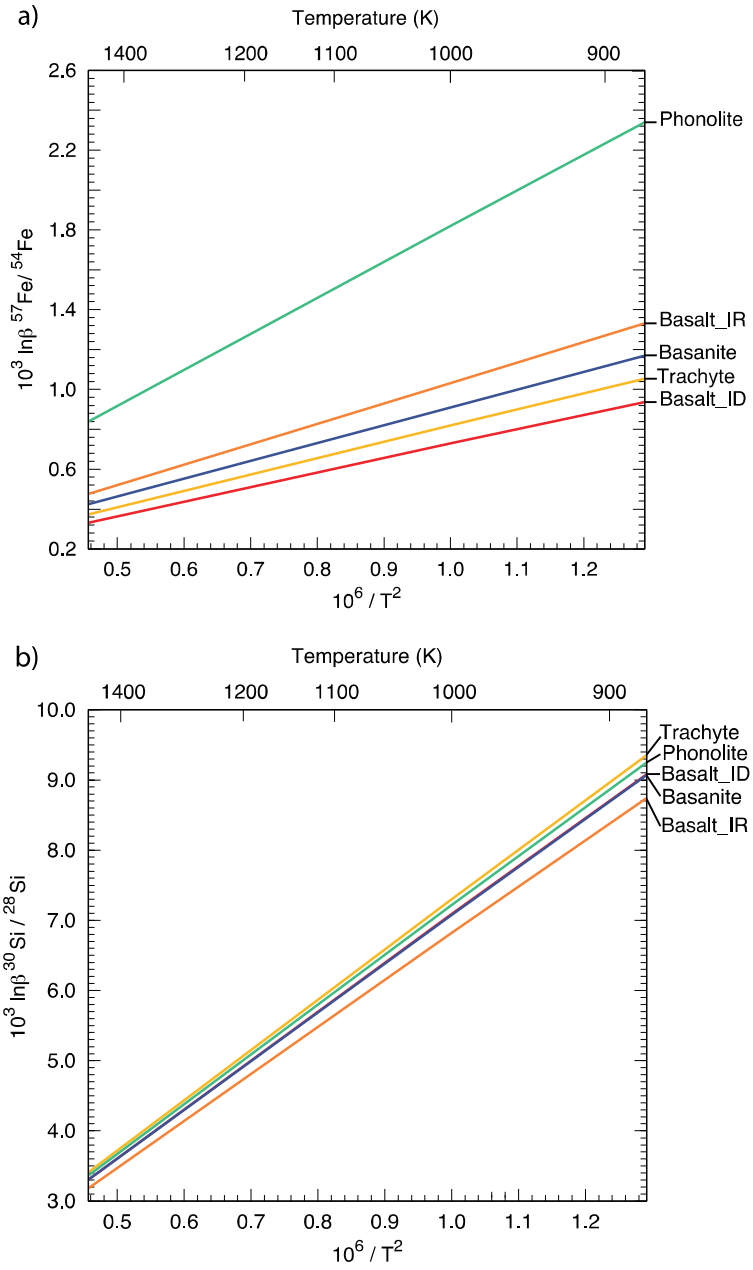

Figure 2 - High-temperature dependence of the reduced partition function ratio for a) iron isotopes and b) silicon isotopes. Basalt_ID and Basalt_IR are the iron-depleted and iron-rich basalt, respectively.

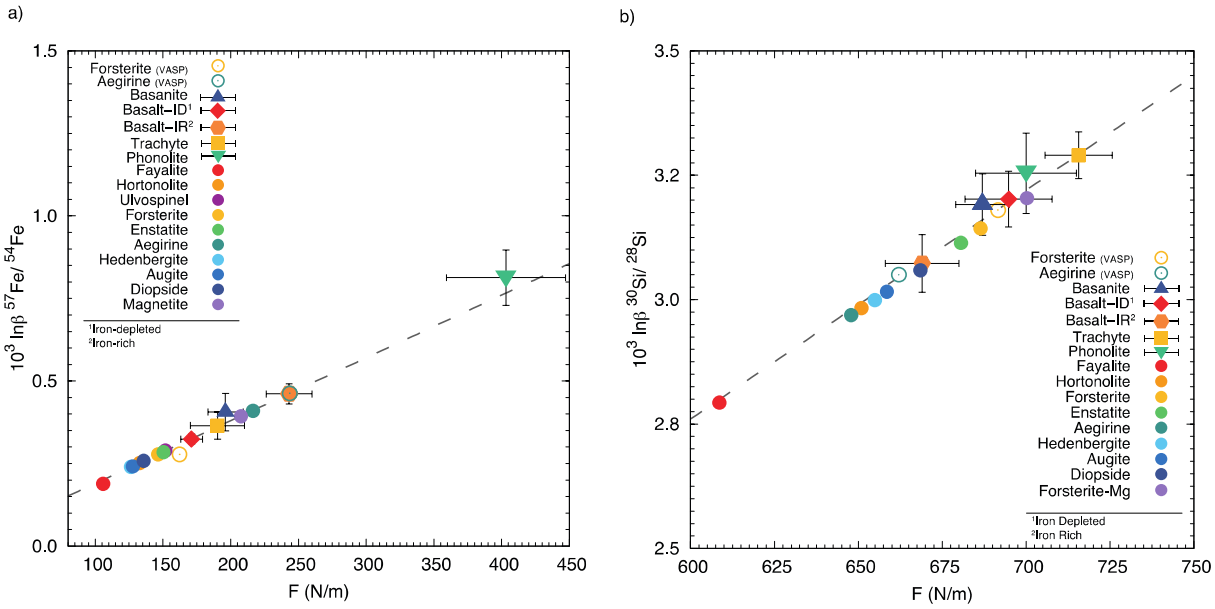

Figure 3 - $10^3 \ln\beta$ *as a function of the average force constant for iron (a) and silicon (b) at T = 1500K. Minerals in plain symbols* $10^3 \ln\beta$ *are taken from the first-principles study of Rabin et al. 2021. The linear fit for iron is f(x) = 0.0019 x for melts and minerals. The linear fit for silicon is f(x) = 0.0046 x for melts and minerals.*

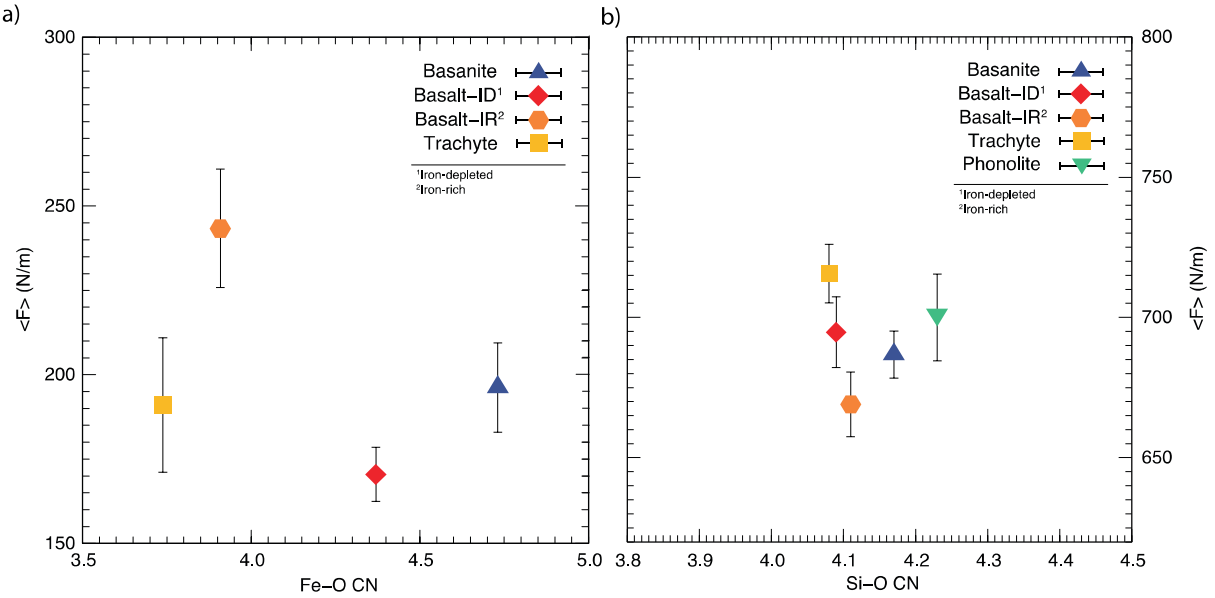

Figure 4 - Relationship between the average force constant and the average coordination number for Fe (a) and Si (b).

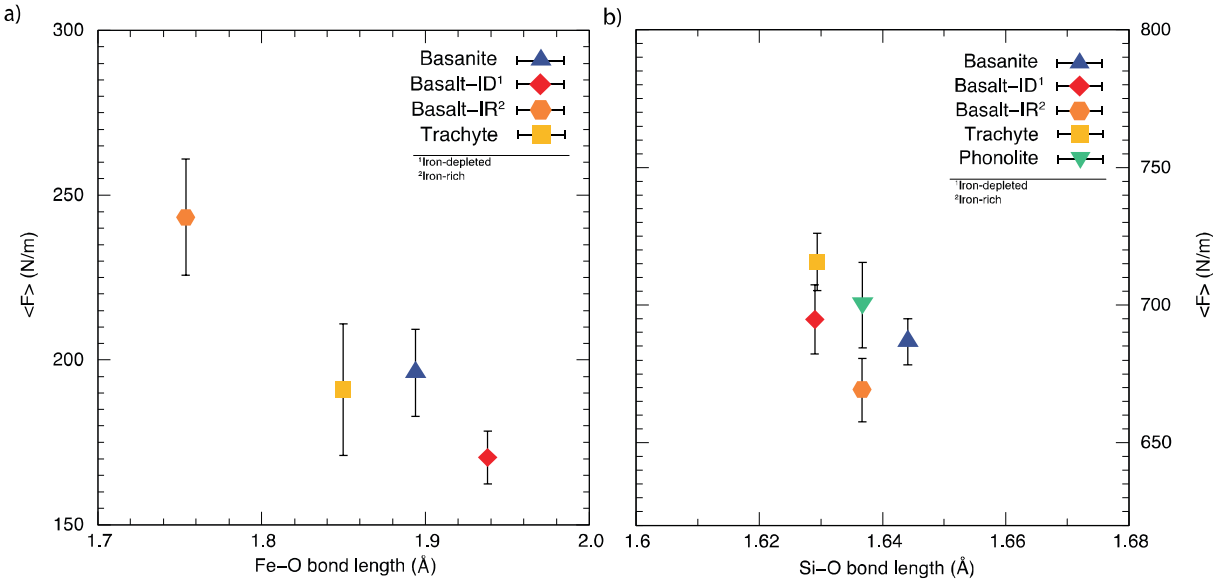

Figure 5 - Relationship between the average force constant and the average bond length for Fe (a) and Si (b).

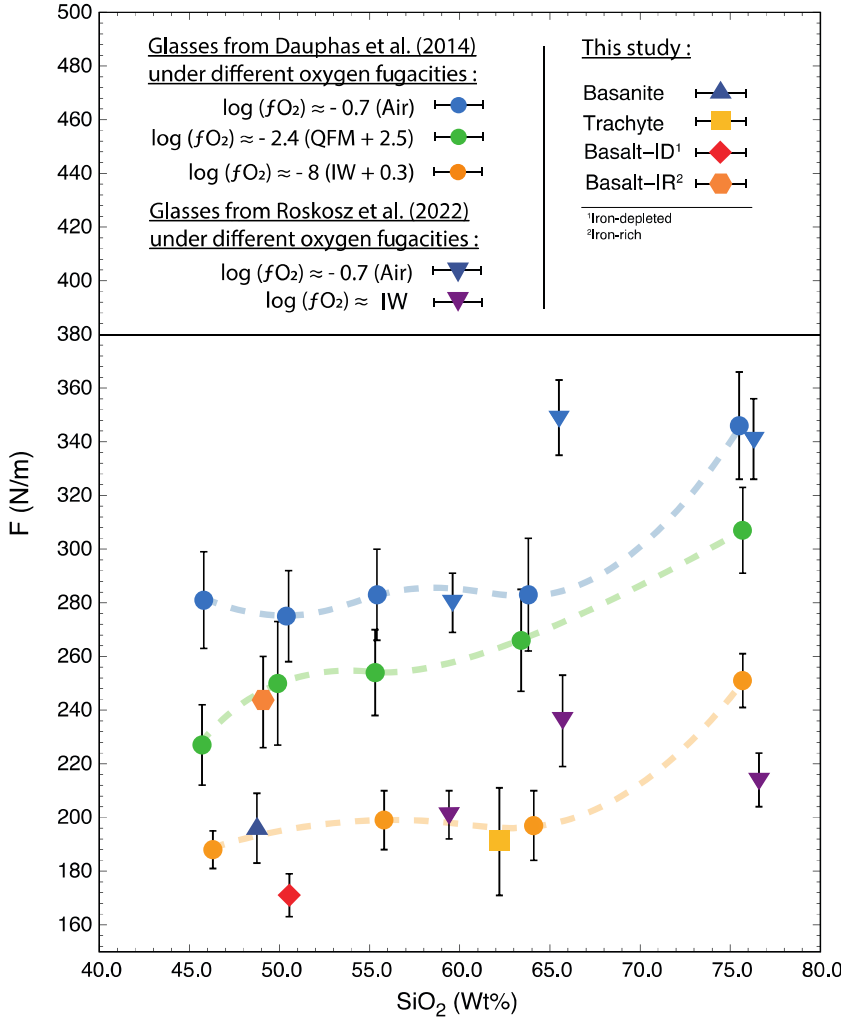

Figure 6 - Comparison of iron force constant of glasses (circles and upside-down triangles) under different oxygen fugacity measured experimentally by Dauphas et al. (2014) and Roskosz et al. (2022) with our calculated iron force constant for the different melts (triangles) versus SiO_2 (in Wt %).

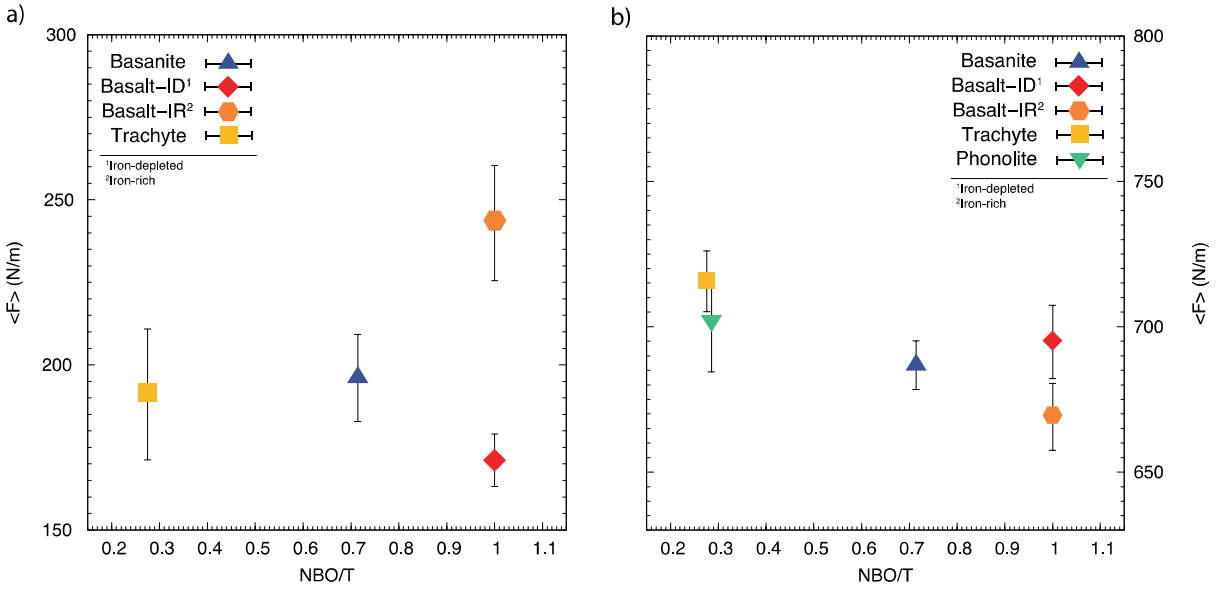

Figure 7 - Relationship between the degree of polymerization (NBO/T) and the Fe force constant (a) or Si force constant (b) of the melts.

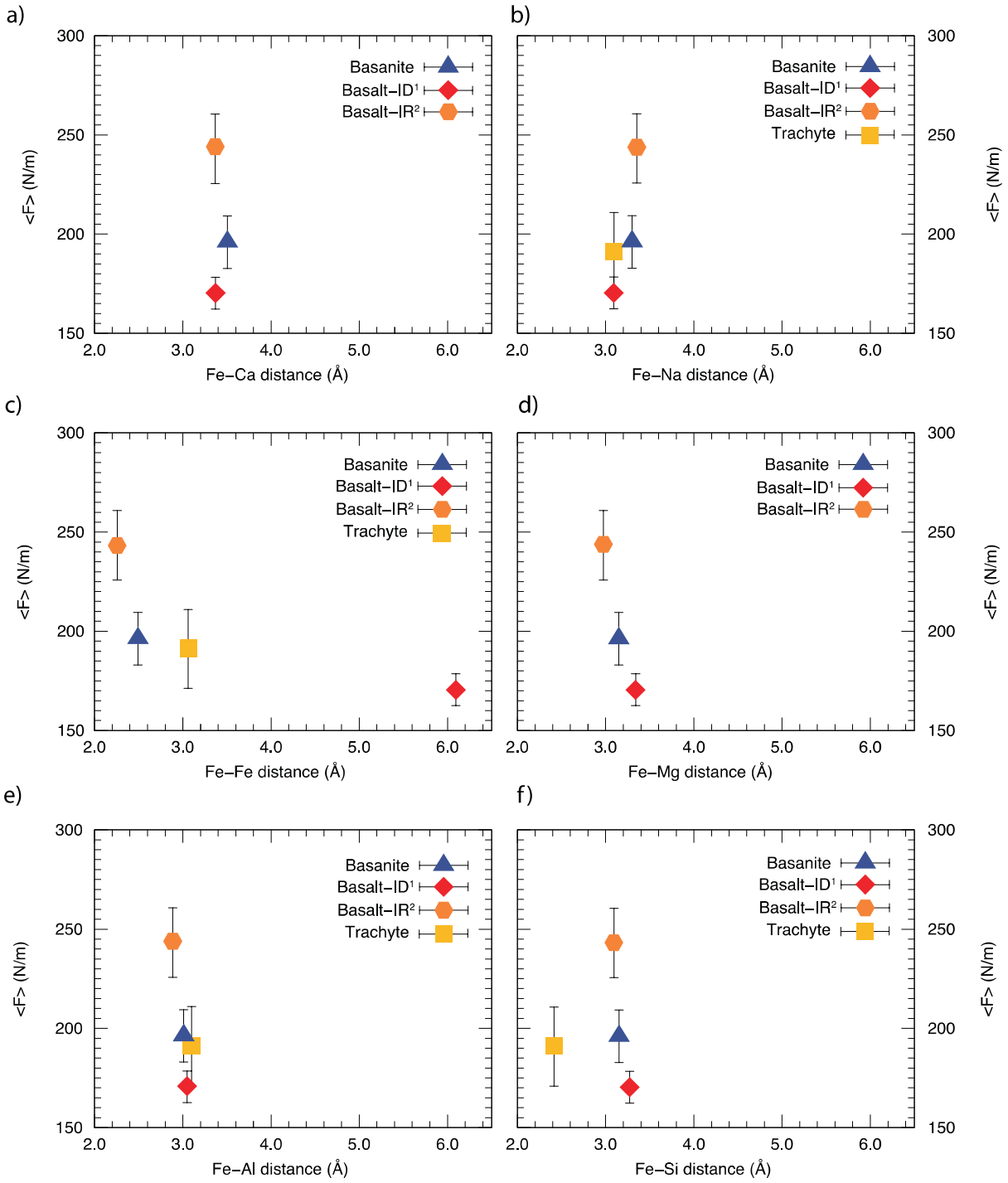

¹Iron-depleted
²Iron-rich

Figure 8 - Relationship between the average Fe-cation distance and the Fe force constant.

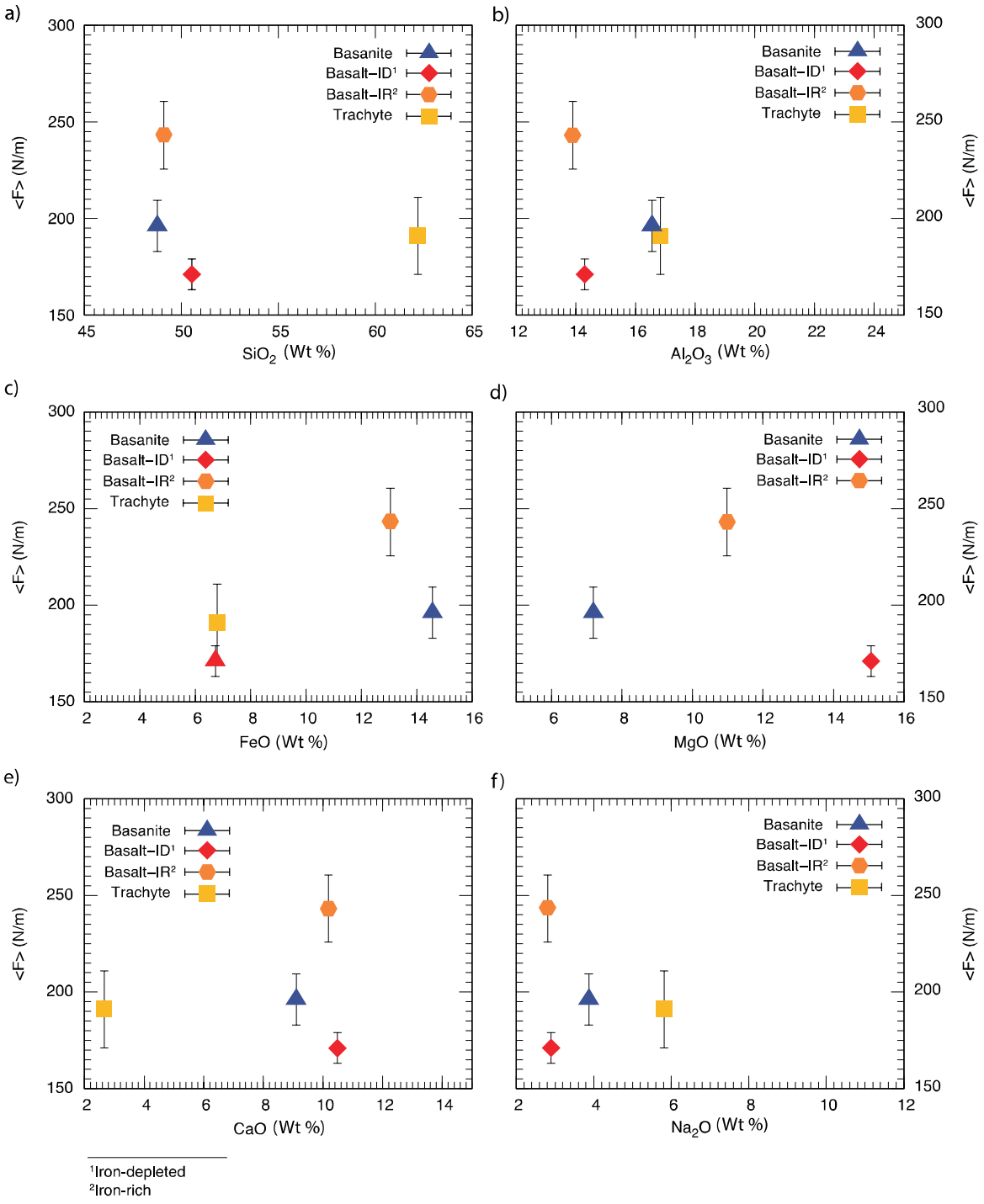

Figure 9 - Relationship between the average iron force constant and the SiO_2 (a), Al_2O_3 (b), FeO (c), MgO (d), CaO (e) and Na_2O (f) content of the melts.

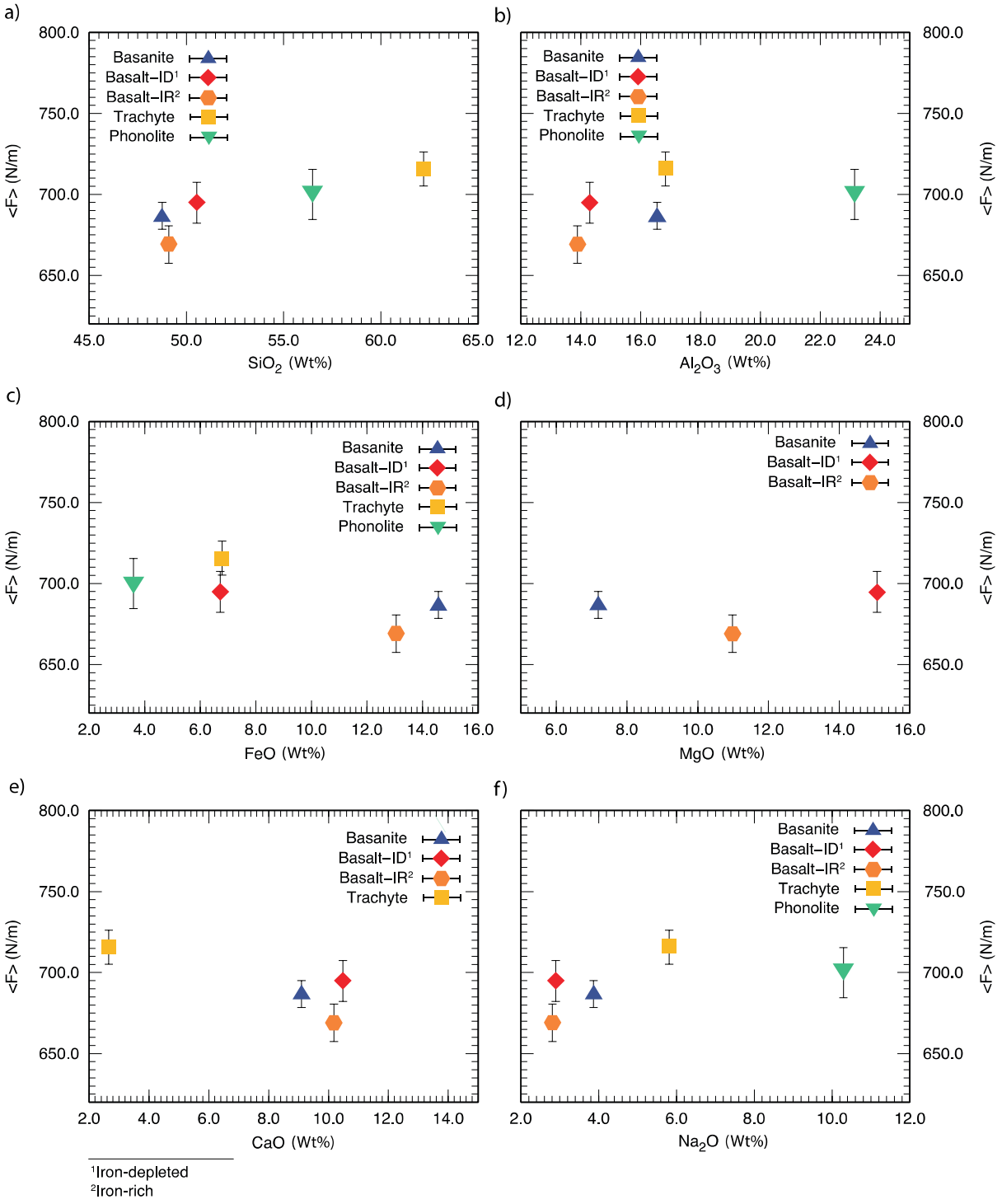

Figure 10 - Relationship between the average silicon force constant and the SiO_2 (a), Al_2O_3 (b), FeO (c), MgO (d), CaO (e) and Na_2O (f) content of the melts.

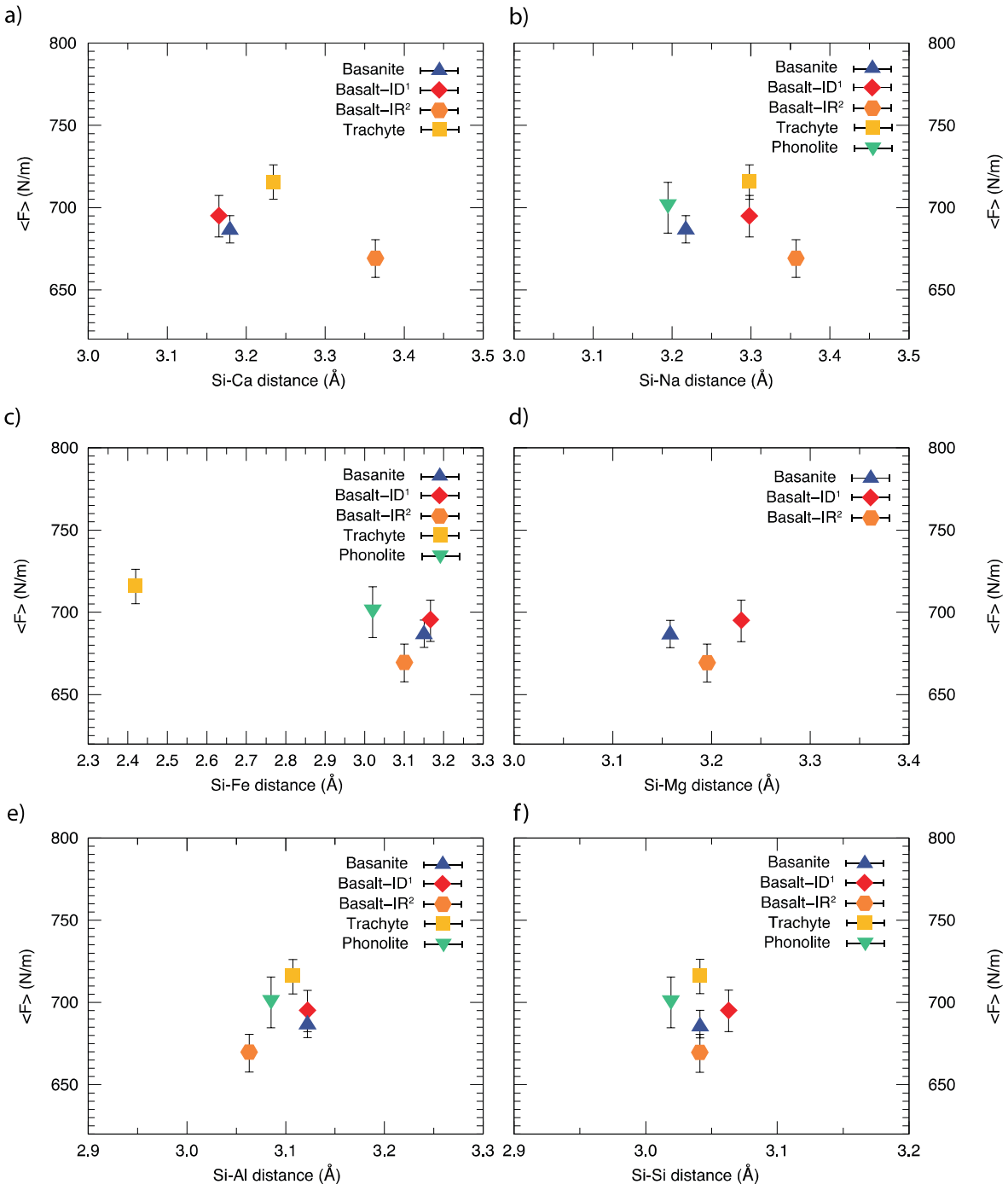

[1]Iron-depleted
[2]Iron-rich

Figure 11 - Relationship between the average Si-cation distance and the Si force constant.

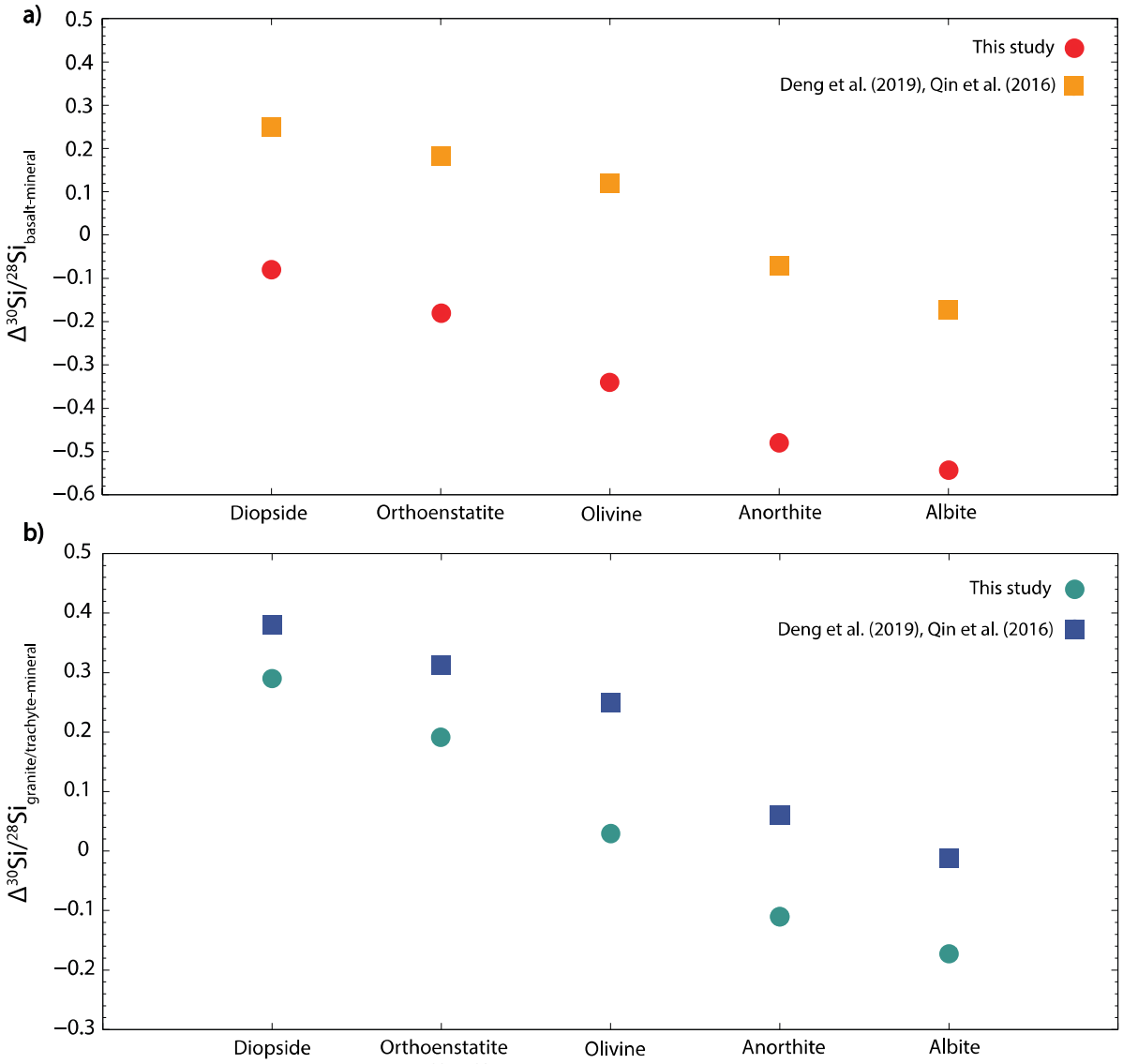

Figure 12 - Comparison between $\Delta_{melt\text{-}mineral}{}^{30}Si/^{28}Si$ calculated in this study and the ones estimated in Deng et al. (2019) from Qin et al. (2016) at 1123 K. The melt β-factors used correspond to the basalt_IR (this study; red) and MORB β-factors (Deng et al. 2019, Qin et al. 2016; orange) in figure a) and to the trachyte (this study; turquoise) and the granite (Deng et al. 2019, Qin et al. 2016; dark blue) β-factors in figure b). The minerals corresponding to the $\Delta_{melt\text{-}mineral}{}^{30}Si/^{28}Si$ are displayed on the x-axis**.** Olivine corresponds here to forsterite (Mg_2SiO_4). The $\Delta_{melt\text{-}mineral}{}^{30}Si/^{28}Si$ displayed in this figure are also available in Table S1 – Appendix B – Supplementary material.

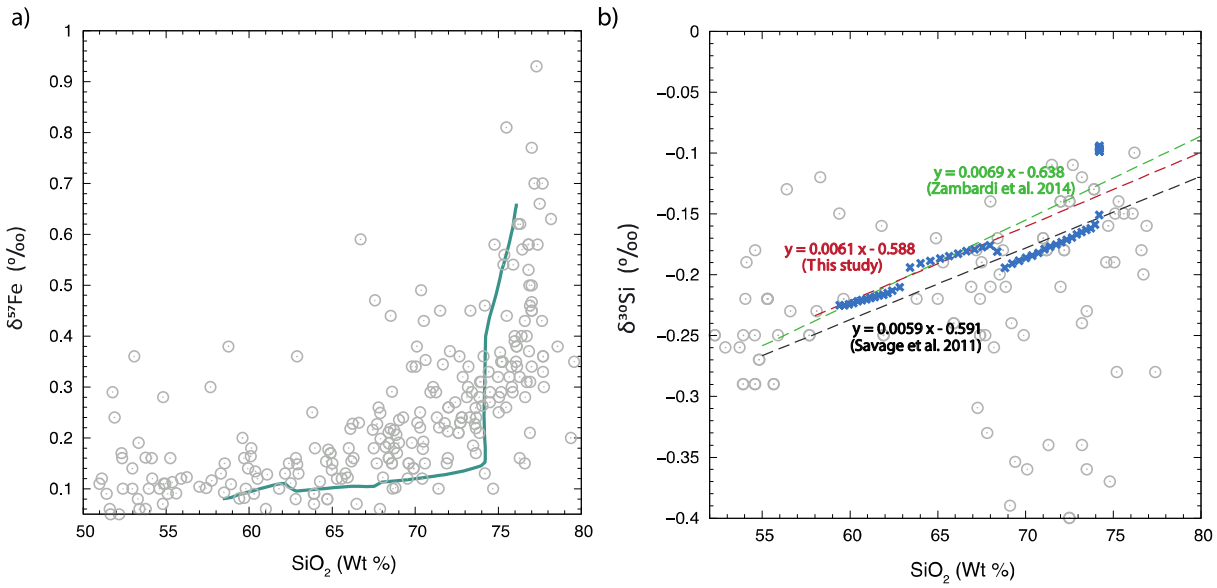

Figure 13 - Models of $\delta^{57}Fe$ (a; blue line) and $\delta^{30}Si$ (b; dark blue cross) evolution during magmatic differentiation : Models were obtained using the MCS software (Bohrson et al., 2014) with starting andesite composition (SiO_2= 58.23, TiO_2 = 0.94, Al_2O_3 = 16.94, Cr_2O_3= 0.03, FeO = 7.31, MgO = 3.99, CaO = 7.08, Na_2O = 3.47, K_2O=1.57, P_2O_5 = 0.24, H_2O = 0.20) with an QFM buffer (Dauphas et al., 2014). Note that the "jumps" in the models correspond to abrupt changes in term of mineralogy during melt differentiation in the MCS software. The grey circles in the background correspond to $\delta^{57}Fe$ (a) and $\delta^{30}Si$ (b) from the literature (Foden et al., 2015; Poitrasson and Freydier, 2005; Savage et al., 2011; Schuessler et al., 2009; Sossi et al., 2012; Telus et al., 2012; Teng et al., 2013; Williams et al., 2018; Zambardi et al., 2014, Savage et al., 2012; Poitrasson and Zambardi, 2015; Du et al., 2017; He et al., 2017; Xia et al., 2017). The fractionation factor $\Delta^{57}Fe_{min\text{-}melt}$ ($\Delta^{57}Fe_{enstatite\text{-}trachyte}$; $\Delta^{57}Fe_{diopside\text{-}trachyte}$; $\Delta^{57}Fe_{ulvospinel\text{-}trachyte}$; $\Delta^{57}Fe_{magnetite\text{-}trachyte}$) and $\Delta^{30}Si_{min\text{-}melt}$ ($\Delta^{30}Si_{enstatite\text{-}trachyte}$; $\Delta^{30}Si_{diopside\text{-}trachyte}$; $\Delta^{30}Si_{anorthite\text{-}trachyte}$; $\Delta^{30}Si_{albite\text{-}trachyte}$; $\Delta^{30}Si_{quartz\text{-}trachyte}$) used in these models are displayed in Table 7. The linear trends in b) represent the linear fit of bulk rock analyses obtained by Savage et al. (2011) in black and Zambardi et al. (2014) in green from natural magmatic rocks analysis as well as the linear trend of our fractional crystallization modelled value (in red).

	nb atoms	V (Å^3)	Density ρ (g/cm^3)	Pressure (GPa)	Temperature (K)
Basalt_IR	100	1341.5	1.64	1.1	4000
Basalt_IR_183	183	2489.52	1.39	0.9	4000
Basalt_IR_HP	100	1079.03	1.98	11.7	4000
Basalt_ID	100	1289.51	1.66	0.7	4000
Basanite	110	1366.48	1.78	1.2	4000
Trachyte	104	1355.82	1.68	1.8	4000
Phonolite	102	1248.44	1.82	0.9	4000

Table 1 - Characteristics of the modeled melts. The pressure given for each melt represents the mean pressure of each FPMD trajectories. The temperature is the target temperature of the FPMD simulations. Basalt_IR_183 and Basalt_IR_HP have the same composition as the iron-rich basalt Basalt_IR with either a larger simulation cell (183 atoms) or a higher pressure (12 GPa). Basalt_ID is the iron depleted basalt.

	Basalt_IR	***Basalt_ID***	***Basanite***	***Trachyte***	***Phonolite***
SiO_2	49.09	50.54	48.75	62.20	56.48
Al_2O_3	13.89	14.30	16.55	16.83	23.15
FeO_T	13.05	6.72	14.57	6.79	3.60
MgO	10.98	15.07	7.19		0.00
CaO	10.18	10.48	9.10	2.66	0.00
Na_2O	2.81	2.90	3.87	5.81	10.29
K_2O	-	-	-	5.71	6.48
Fe mean valence	2.3	2.37	2.36	2.33	2.28
NBO/T	1	1	0.71	0.29	0.28

Table 2 - Composition in wt % and degree of polymerization (NBO/T) of the modeled melts as well as the mean valence of iron atoms in the melts that correspond to the Born effective charge calculated in VASP. See Table 1 for sample denomination.

	Ca-O		**Na-O**		**K-O**		**Fe-O**		**Mg-O**		**Al-O**		**Si-O**	
	CN	d(Å)	CN	d(Å)	CN	d(Å)	CN	d(Å)	CN	d(Å)	CN	d(Å)	CN	d(Å)
Basalt_IR	6.92	2.28	6.55	2.30	-	-	3.91	1.76	5.31	1.99	4.57	1.77	4.11	1.64
Basalt_183	6.88	2.26	6.43	2.28	-	-	3.95	1.78	5.25	1.97	4.49	1.77	4.07	1.64
Basalt_HP	9.53	2.24	9.27	2.24	-	-	5.08	1.80	7.12	1.95	5.45	1.76	4.64	1.64
Basalt_ID	6.95	2.28	6.24	2.35	-	-	4.37	1.94	5.27	1.99	4.59	1.77	4.09	1.63
Basanite	7.48	2.31	7.76	2.30	-	-	4.73	1.90	5.32	1.98	4.75	1.77	4.17	1.64
Trachyte	6.49	2.25	6.80	2.32	10.28	2.68	3.74	1.85	-	-	4.66	1.81	4.08	1.63
Phonolite	-	-	7.71	2.25	11.42	2.65	5.11	1.63	-	-	4.73	1.78	4.23	1.64

Table 3 - Cation-oxygen coordination number as well as the average cation-oxygen bond length of the modeled melts. See Table 1 for sample denomination.

	Basalt_IR		Basalt_ID		Basanite		Trachyte		Phonolite	
	d(Å)	CN	d(Å)	CN	d(Å)	CN	d(Å)	CN	d(Å)	CN
Fe-Ca	3.37	1.27	3.37	1.13	3.50	1.49	-	-	-	-
Fe-Na	3.35	0.64	3.09	1.14	3.30	0.91	3.09	0.63	3.09	1.27
Fe-K	-	-	-	-	-	-	-	-	3.59	2.07
Fe-Fe	2.25	1.21	6.09	-	2.49	1.24	3.06	-	-	-
Fe-Mg	2.98	1.43	3.34	2.07	3.15	1.05	-	-	-	-
Fe-Al	3.10	1.06	3.05	1.29	3.01	1.79	3.10	1.68	3.17	3.09
Fe-Si	3.09	3.02	3.08	4.06	3.15	4.19	2.97	4.11	3.00	4.30
Si-Ca	3.36	1.30	3.17	1.38	3.26	1.11	3.24	0.37	-	-
Si-Na	3.36	0.76	3.30	0.51	3.22	1.16	3.30	1.17	3.20	2.49
Si-Fe	3.09	0.68	3.10	0.56	3.15	1.21	2.95	0.38	3.02	0.22
Si-Mg	3.20	1.70	3.23	1.80	3.15	1.02	-	-	-	-
Si-Al	3.06	1.30	3.12	0.65	3.12	1.56	3.11	1.42	3.09	1.69
Si-Si	3.04	2.36	3.06	1.22	3.04	2.31	3.04	2.88	3.02	2.81
Si-K	-	-	-	-	-	-	3.58	2.16	3.50	2.80

Table 4 - Iron-cation and silicon-cation coordination numbers and their corresponding average distance in the modeled melts. See Table 1 for sample denomination.

	$10^3 \ln \beta\ ^{57}Fe/^{54}Fe$			$10^3 \ln \beta\ ^{30}Si/^{28}Si$			
	A	B	Value at 1500 K	A	B	C	Value at 1500 K
Basalt_IR	-0.0059	1.0332	0.461 ± 0.031	0.0028	-0.1474	6.9342	3.073 ± 0.058
Basalt_ID	-0.0035	0.7269	0.324 ± 0.015	0.0031	-0.1569	7.2036	3.202 ± 0.056
Basanite	-0.0061	0.8986	0.406 ± 0.057	0.0031	-0.1578	7.1926	3.191 ± 0.062
Trachyte	-0.0044	0.8178	0.365 ± 0.041	0.0033	-0.165	7.4202	3.290 ± 0.047
Phonolite	-0.0155	1.8063	0.813 ± 0.084	0.0033	-0.1643	7.334	3.254 ± 0.081

Table 5 - Polynomial fits of the reduced partition function ratios for $^{57}Fe/^{54}Fe$ and $^{30}Si/^{28}Si$. Polynomial fits use equation of type $Ax^2 + Bx$ for $10^3 \ln\beta\ ^{57}Fe\text{-}^{54}Fe$ and $Ax^3 + Bx^2 + Cx$ for $10^3 \ln\beta\ ^{30}Si\text{-}^{28}Si$ with $x = 10^6/T^2$ for T between 0 and 1500 K. See Table 1 for sample denomination.

	Fe force constant		**Si force constant**
	« Snapshot » method	« VAF » method	« Snapshot » method
Basalt_IR	243 ± 17	235 ± 24	669 ± 11
Basalt_ID	171 ± 8	193 ± 19	695 ± 13
Basanite	196 ± 13	196 ± 23	687 ± 8
Phonolite	403 ± 44	290 ± 99	700 ± 15
Trachyte	191 ± 20	159 ± 38	716 ± 10
Basalt_HP	-	269 ± 33	-
Basalt_183	-	222 ± 12	-

Table 6 - Comparison of the iron average force constants of the melts (in N/m) using either the “snapshot” method or the “VAF” method as well as the silicon force constants of the melts using the “snapshot” method. See Table 1 for sample denomination.

$\Delta_{A\text{-}B}$ $^{57}Fe/^{54}Fe$					$\Delta_{A\text{-}B}$ $^{29}Si/^{30}Si$				
	C_1	C_2	at 1500 K			C_1	C_2	C_3	at 1500 K
$\Delta_{Aegirine\text{-}Basalt\_IR}$	0.0013	-0.0081	-0.003 ±	0.04	$\Delta_{Aegirine\text{-}Basalt\_IR}$	-0.0003	0.0128	-0.1088	-0.046 ± 0.15
$\Delta_{Enstatite\text{-}Basalt\_IR}$	0.0028	-0.32	-0.142 ±	0.03	$\Delta_{Enstatite\text{-}Basalt\_IR}$	0.0001	-0.0029	0.229	0.101 ± 0.16
$\Delta_{Forsterite\text{-}Basalt\_IR}$	0.0036	-0.3385	-0.150 ±	0.03	$\Delta_{Forsterite\text{-}Basalt\_IR}$	0.0004	-0.0035	0.2951	0.130 ± 0.16
$\Delta_{Augite\text{-}Basalt\_IR}$	0.0038	-0.4266	-0.189 ±	0.03	$\Delta_{Augite\text{-}Basalt\_IR}$	-0.0002	0.0077	0.0022	0.002 ± 0.15
$\Delta_{Hortonolite\text{-}Basalt\_IR}$	0.0039	-0.4042	-0.179 ±	0.03	$\Delta_{Hortonolite\text{-}Basalt\_IR}$	-0.0003	0.01	0.074	0.035 ± 0.15
$\Delta_{Hedenbergite\text{-}Basalt\_IR}$	0.0043	-0.4329	-0.192 ±	0.03	$\Delta_{Hedenbergite\text{-}Basalt\_IR}$	-0.0002	0.0067	-0.0376	-0.015 ± 0.15
$\Delta_{Fayalite\text{-}Basalt\_IR}$	0.0047	-0.5601	-0.248 ±	0.03	$\Delta_{Fayalite\text{-}Basalt\_IR}$	-0.0007	0.0268	-0.515	-0.224 ± 0.14
$\Delta_{Diopside\text{-}Basalt\_IR}$	0.0039	-0.3884	-0.172 ±	0.03	$\Delta_{Diopside\text{-}Basalt\_IR}$	0.0004	0.000009	0.1026	0.046 ± 0.16
$\Delta_{Ulvospinel\text{-}Basalt\_IR}$	0.0033	-0.3104	-0.137 ±	0.03	$\Delta_{Forsterite\text{-}Mg\text{-}Basalt\_IR}$	0.0001	-0.0092	0.4385	0.193 ± 0.16
$\Delta_{Magnetite\text{-}Basalt\_IR}$	0.0023	-0.0476	-0.021 ±	0.04	$\Delta_{Quartz\text{-}Basalt\_IR}$	0.0062	-0.0694	0.7804	0.334 ± 0.17
					$\Delta_{Anorthite\text{-}Basalt\_IR}$	0.0059	-0.066	0.7351	0.314 ± 0.17
					$\Delta_{Albite\text{-}Basalt\_IR}$	0.0055	-0.0609	0.6467	0.276 ± 0.171
$\Delta_{Aegirine\text{-}Basalt\_ID}$	-0.0011	0.2982	0.132 ±	0.03	$\Delta_{Aegirine\text{-}Basalt\_ID}$	-0.0006	0.0223	-0.3782	-0.164 ± 0.15
$\Delta_{Enstatite\text{-}Basalt\_ID}$	0.0004	-0.0137	-0.006 ±	0.02	$\Delta_{Enstatite\text{-}Basalt\_ID}$	-0.0002	0.0066	-0.0404	-0.017 ± 0.16
$\Delta_{Forsterite\text{-}Basalt\_ID}$	0.0012	-0.0322	-0.014 ±	0.02	$\Delta_{Forsterite\text{-}Basalt\_ID}$	-0.0003	0.006	0.0257	0.013 ± 0.16
$\Delta_{Augite\text{-}Basalt\_ID}$	0.0014	-0.1203	-0.053 ±	0.02	$\Delta_{Augite\text{-}Basalt\_ID}$	-0.0005	0.0172	-0.2672	-0.115 ± 0.15
$\Delta_{Hortonolite\text{-}Basalt\_ID}$	0.0015	-0.0979	-0.043 ±	0.02	$\Delta_{Hortonolite\text{-}Basalt\_ID}$	-0.0006	0.0195	-0.3434	-0.149 ± 0.15
$\Delta_{Hedenbergite\text{-}Basalt\_ID}$	0.0019	-0.1266	-0.056 ±	0.02	$\Delta_{Hedenbergite\text{-}Basalt\_ID}$	-0.0005	0.0162	-0.307	-0.133 ± 0.15
$\Delta_{Fayalite\text{-}Basalt\_ID}$	0.0023	-0.2538	-0.112 ±	0.02	$\Delta_{Fayalite\text{-}Basalt\_ID}$	-0.001	0.0363	-0.7844	-0.342 ± 0.14
$\Delta_{Diopside\text{-}Basalt\_ID}$	0.0015	-0.0821	-0.036 ±	0.02	$\Delta_{Diopside\text{-}Basalt\_ID}$	-0.0003	0.0095	-0.1668	-0.072 ± 0.15
$\Delta_{Ulvospinel\text{-}Basalt\_ID}$	0.0009	-0.0041	-0.002 ±	0.02	$\Delta_{Forsterite\text{-}Mg\text{-}Basalt\_ID}$	-0.0002	0.0003	0.1691	0.075 ± 0.16
$\Delta_{Magnetite\text{-}Basalt\_ID}$	-0.000056	0.258656	0.115 ±	0.03	$\Delta_{Quartz\text{-}Basalt\_ID}$	0.0059	-0.0599	0.511	0.216 ± 0.17
					$\Delta_{Anorthite\text{-}Basalt\_ID}$	0.0052	-0.0514	0.3773	0.158 ± 0.17
					$\Delta_{Albite\text{-}Basalt\_ID}$	0.0056	-0.0565	0.4657	0.196 ± 0.17
$\Delta_{Aegirine\text{-}Basanite}$	0.0015	0.1265	0.057 ±	0.06	$\Delta_{Aegirine\text{-}Basanite}$	-0.0006	0.0232	-0.3672	-0.159 ± 0.16
$\Delta_{Enstatite\text{-}Basanite}$	0.003	-0.1854	-0.082 ±	0.06	$\Delta_{Enstatite\text{-}Basanite}$	-0.0002	0.0075	-0.0294	-0.012 ± 0.17
$\Delta_{Forsterite\text{-}Basanite}$	0.0038	-0.2039	-0.090 ±	0.06	$\Delta_{Forsterite\text{-}Basanite}$	-0.0003	0.0069	0.0367	0.018 ± 0.17
$\Delta_{Augite\text{-}Basanite}$	0.004	-0.292	-0.129 ±	0.06	$\Delta_{Augite\text{-}Basanite}$	-0.0005	0.0181	-0.2562	-0.110 ± 0.16
$\Delta_{Hortonolite\text{-}Basanite}$	0.0041	-0.2538	-0.112 ±	0.06	$\Delta_{Hortonolite\text{-}Basanite}$	-0.0006	0.0204	-0.3324	-0.144 ± 0.16
$\Delta_{Hedenbergite\text{-}Basanite}$	0.0045	-0.2983	-0.132 ±	0.06	$\Delta_{Hedenbergite\text{-}Basanite}$	-0.0005	0.0171	-0.296	-0.128 ± 0.16
$\Delta_{Fayalite\text{-}Basanite}$	0.0049	-0.4255	-0.188 ±	0.06	$\Delta_{Fayalite\text{-}Basanite}$	-0.001	0.0372	-0.7734	-0.336 ± 0.15
$\Delta_{Diopside\text{-}Basanite}$	0.0041	-0.2538	-0.112 ±	0.06	$\Delta_{Diopside\text{-}Basanite}$	-0.0003	0.0104	-0.1558	-0.067 ± 0.16
$\Delta_{Ulvospinel\text{-}Basanite}$	0.0035	-0.1758	-0.077 ±	0.06	$\Delta_{Forsterite\text{-}Mg\text{-}Basanite}$	-0.0002	0.0012	0.1801	0.080 ± 0.17
$\Delta_{Magnetite\text{-}Basanite}$	0.0025	0.087	0.039 ±	0.06	$\Delta_{Quartz\text{-}Basanite}$	0.0059	-0.059	0.522	0.221 ± 0.18
					$\Delta_{Anorthite\text{-}Basanite}$	0.0052	-0.0505	0.3883	0.163 ± 0.18
					$\Delta_{Albite\text{-}Basanite}$	0.0056	-0.056	0.4767	0.201 ± 0.18

Table 7 - Polynomial fits of iron and silicon fractionation factors between various minerals and melts. Polynomial fits use equation of type $C_1x^2 + C_2x$ for $\Delta^{57}Fe\text{-}^{54}Fe$ and $C_1x^3 + C_2x^2 + C_3x$ for $\Delta^{30}Si\text{-}^{28}Si$ with $x = 10^6/T^2$ for T between 0 and 1500 K. The iron and silicon β-factor of minerals were taken from Rabin et al. (2021) for all minerals except quartz, albite and anorthite that were taken from Qin et al. (2016).

$\Delta_{A\text{-}B}$ $^{57}Fe/^{54}Fe$				$\Delta_{A\text{-}B}$ $^{29}Si/^{30}Si$				
A	C_1	C_2	at 1500 K	A	C_1	C_2	C_3	at 1500 K
$\Delta_{Aegirine\text{-}Trachyte}$	-0.0002	0.2073	0.092 ± 0.05	$\Delta_{Aegirine\text{-}Trachyte}$	-0.0008	0.0304	-0.5948	-0.258 ± 0.15
$\Delta_{Enstatite\text{-}Trachyte}$	0.0013	-0.1046	-0.046 ± 0.04	$\Delta_{Enstatite\text{-}Trachyte}$	-0.0004	0.0147	-0.257	-0.111 ± 0.16
$\Delta_{Forsterite\text{-}Trachyte}$	0.0021	-0.1231	-0.054 ± 0.04	$\Delta_{Forsterite\text{-}Trachyte}$	-0.0005	0.0141	-0.1909	-0.082 ± 0.16
$\Delta_{Augite\text{-}Trachyte}$	0.0023	-0.2112	-0.093 ± 0.04	$\Delta_{Augite\text{-}Trachyte}$	-0.0007	0.0253	-0.4838	-0.210 ± 0.16
$\Delta_{Hortonolite\text{-}Trachyte}$	0.0024	-0.1888	-0.083 ± 0.04	$\Delta_{Hortonolite\text{-}Trachyte}$	-0.0008	0.0276	-0.56	-0.244 ± 0.15
$\Delta_{Hedenbergite\text{-}Trachyte}$	0.0028	-0.2175	-0.096 ± 0.04	$\Delta_{Hedenbergite\text{-}Trachyte}$	-0.0007	0.0243	-0.5236	-0.228 ± 0.16
$\Delta_{Fayalite\text{-}Trachyte}$	0.0032	-0.3447	-0.153 ± 0.04	$\Delta_{Fayalite\text{-}Trachyte}$	-0.0012	0.0444	-1.001	-0.436 ± 0.15
$\Delta_{Diopside\text{-}Trachyte}$	0.0024	-0.173	-0.076 ± 0.04	$\Delta_{Diopside\text{-}Trachyte}$	-0.0005	0.0176	-0.3834	-0.167 ± 0.16
$\Delta_{Ulvospinel\text{-}Trachyte}$	0.0018	-0.095	-0.042 ± 0.04	$\Delta_{Forsterite\text{-}Mg\text{-}Trachyte}$	-0.0004	0.0084	-0.0475	-0.019 ± 0.17
$\Delta_{Magnetite\text{-}Trachyte}$	0.0008	0.1678	0.075 ± 0.05	$\Delta_{Quartz\text{-}Trachyte}$	0.0057	-0.0518	0.2944	0.121 ± 0.17
				$\Delta_{Anorthite\text{-}Trachyte}$	0.005	-0.0433	0.1607	0.063 ± 0.17
				$\Delta_{Albite\text{-}Trachyte}$	0.0054	-0.0484	0.2491	0.102 ± 0.17

Table 7 – Suite.